NURail Project
NURail2012-UIC-R01-combined

The final report for NURail project: **NURail2012-UIC-R01** consists of two distinct documents.

- Section 1, 24 pages, titled “Modeling of Rail Track Substructure Linear Elastic Coupling”, written by Craig Foster, Ahmed El-Ghandour and Martin B. Hamper

- Section 2, 42 pages, titled “Modeling of Rail Track Substructure Soil Plasticity Modeling”, written by Craig Foster and Mohammad Hosein Motamedi

These were completed under grant number: DTRT12-G-UTC18.

National University Rail Center - NURail
US DOT OST-R Tier 1 University Transportation Center

NURail Project ID: NURail2012-UIC-R01-A

Modeling of Rail Track Substructure
Linear Elastic Coupling

By

Craig Foster
Associate Professor
Department of Civil and Materials Engineering
University of Illinois at Chicago
fosterc@uic.edu

Ahmed El-Ghandour
Graduate Research Assistant
Department of Civil and Materials Engineering
University of Illinois at Chicago
aelgha2@uic.edu

Martin B. Hamper
PhD, Mechanical Engineering
University of Illinois at Chicago
Research Engineer
Toyota Technical Center
Ann Arbor, Michigan
martinhamper@gmail.com

30-09-2015

Grant Number: DTRT12-G-UTC18

DISCLAIMER

Funding for this research was provided by the NURail Center, University of Illinois at Urbana - Champaign under Grant No. DTRT12-G-UTC18 of the U.S. Department of Transportation, Office of the Assistant Secretary for Research & Technology (OST-R), University Transportation Centers Program. The contents of this report reflect the views of the authors, who are responsible for the facts and the accuracy of the information presented herein. This document is disseminated under the sponsorship of the U.S. Department of Transportation's University Transportation Centers Program, in the interest of information exchange. The U.S. Government assumes no liability for the contents or use thereof.

National University Rail Center - NURail
US DOT OST-R Tier 1 University Transportation Center

TECHNICAL SUMMARY

Title

Modeling of Rail Track Substructure – Linear Elastic Coupling

Introduction

Most analyses of rail dynamics neglect contribution of the soil, or treat it in a very simple manner such as using spring elements. This can cause accuracy issues in examining dynamics for passenger comfort, derailment, substructure analysis, or other reasons. We examine how the treatment of the soil in a continuum fashion influences rail simulations.

Approach and Methodology

We use the finite element method to build a continuum model of the track structure and soil, including rails, fasteners, crossties (sleepers), ballast, subballast, and subgrade. We export the modal stiffness of the track structure to a multibody code to simulate the wheel/rail contact of a train over the track. From the modal displacements, the nodal displacements can be reconstructed in the finite element model. Contact forces and other quantities of interest can be determined.

Findings

The above methodology was able to produce similar results to existing formulations that used linear spring-dampers for the soil. A large number of modes, typically 100-300, were needed to get an accurate solution. There were some differences with respect to simpler formualtions, notably that depression of a tie can, by Poisson effects, create a rise in adjacent ties.

Conclusions

Coupled finite element and multibody dynamics simulations can be used to simulate the entire track system including the substructure. Modal decomposition of the substructure, in the linear case, can create an accurate model with little extra computational effort in the multibody simulation. Quantities of interest can then be reconstructed. Some differences are noticed when compared to simplified models, suggesting that this type of model may be needed even when the substructure is not the focus of the study.

Recommendations

It is recommended that a full continuum representation of track substructure be used when soil deformation significantly affects track movement, or when the motion of the substructure is important.

Publications

A.I. El-Ghandour, M.B. Hamper, and C.D. Foster. "Coupled Finite Element and Multibody Dynamics Systems Modeling of a 3D railroad system". *Journal of Rail and Rapid Transit*, In press.

Primary Contact
Principal Investigator
Craig D. Foster
Associate Professor
Department of Civil and Materials Engineering
University of Illinois at Chicago
312-996-8086
foster@uic.edu

Other Faculty and Students Involved
Ahmed I. El-Ghandour
Research Assistant
Department of Civil and Materials Engineering
University of Illinois at Chicago
312-996-0438
aelgha2@uic.edu

Martin B. Hamper
Engineer
Toyota Technical Center
martinhamper@gmail.com
773-396-7066

Thanakorn Siriaksorn
Research Assistant
Department of Civil and Materials Engineering
University of Illinois at Chicago
312-996-6725
tsiria3@uic.edu

NURail Center
217-244-4999
nurail@illinois.edu
http://www.nurailcenter.org/

TABLE OF CONTENTS

TABLE

pppp

LIST OF FIGURES

1 INTRODUCTION

During the last two centuries, railroad vehicles have been one of the most important transportation methods for both people and cargo. They are a highly economical means of transporting large quantities of cargo over long distances and also provide a safe and comfortable means of passenger transport. In the nearly five decades since Japan first introduced them for the 1964 Olympics, the use of high speed trains has significantly increased in many countries all over the world as they save time for the passengers. However, the increase of the speed requires that extra research be carried out to guarantee passenger safety and comfort.

The rail system consists of different components, including the vehicle and the rails, which are in contact through the wheel/rail interface. The sleepers (also known as cross ties) maintain the correct spacing (gage) between the rails, and transmit the vertical load from the vehicle to the ballast and sub-grade. Sleepers are connected to the rails and the ground through fasteners. The ground itself consists of three layers: ballast, sub-ballast, and sub-grade. Ballast is a granular layer that assists in holding the sleepers in position and transfers the load to the lower layers. Sub-ballast and sub-grade layers help by supporting the ballast and the above components (AREMA manual [1], Shabana et al [2]). Dynamically, all of these elements work to transfer the load of the vehicle to the ground in a way that ensures smooth operation and minimizes wear and maintenance on components. Due to the importance of rail systems, many investigations have been dedicated to providing models that can assist in the understanding and avoidance of problems such as: derailments (Barbosa [3], Sato et al [4], Wang and Li [5]), ballast settlement (Huang and Tutumluer [6], Brown et al [7]), unsupported sleepers (Zhang et al [8], Recuero et al [9], Lundqvist and Dahlberg [10]), and other problems.

The finite element method (FEM) is a tool commonly used for modeling and investigating the rails and the other components mentioned above. For instance, Sladkowski and Sitarz [11] analyzed the interaction between the wheel and the rail using FEM. Sladkowski and Sitarz compared different wheel and rail profiles to analyze the stresses in each of them, and studied which ones might wear less, and how the different rail profiles perform with the different wheel profiles. Monfared [12] used FEM to investigate the stress produced due to the contact between the wheel and rail. He performed a static analysis to predict the critical points, i.e. the points of highest stress. These points may be on the contact surface of the rail or the wheel or in the rail web (the part between the rail head and rail bottom). Although the model included only the wheel and the rail, the investigation covered different contact patch shapes such as: elliptical, rectangular, and circular. Arslan and Kayabas [13] also used FEM to model the wheel and rails in the contact problem. The main concern of their work was to provide a detailed process of how to build a realistic FE 3D model, including the loads and boundary conditions.

Many numerical models have assumed that the substructure is rigid, although some take into account the flexibility of the rail itself. Sometimes the elasticity of ballast, which is an essential component in the railroad system, is modeled using spring-damper elements. Xiao et al [14] included the ballast in their work to study what can happen due to track support failures. The ballast and the sub-grade are modeled as spring-damper elements. The results showed the effect of the support failure on the vehicle's dynamic response. In Xiao et al [15], a similar model was used in that case of curved track in order to investigate the effect of track support failure on the train derailment during curve negotiations.

On the other hand, full continuum finite elements have been used instead of spring-damper elements in some investigations to model the different substructure layers. Kumaran et al [16] used FEM for

modeling the rail, sleepers, ballast and sub-ballast to investigate the wheel/rail interaction and the effect of the dynamic response of prestressed concrete sleeper. The dynamic response was investigated for a high-speed train by Chebli et al [17] where FEM was used to build a model to investigate the in situ measurements. Another FE model was presented by Koskinen [18] to model the railway, bridge, and soil interaction and study the effect of the substructure on the rails.

Recently, the discrete element method (DEM) has been used to investigate ballast settlement, which can cause uneven displacement of the rail and reduce the smoothness of the train ride. This effect can, in turn, increase wear and even cause derailment of the vehicle. Tutumluer et al [19] used DEM to investigate this problem, by studying different ballast properties, such as aggregate type, angularity, and gradation. The results of their work show that increasing the load leads to an increase in the plastic deformation. While discrete elements are useful in determining the behavior of different gravels, they are too computationally expensive at this time to efficiently couple directly to finite element (FE) analysis of wheel and rail behavior.

In addition to the finite element method, multibody systems (MBS) codes are very important tools in different mechanical systems and have been used by many researchers in different fields such as vehicle analysis, rotor dynamics, and turbine gearboxes (Busch and Schweizer [20], Ibrahimbegović et al [21], and Heege et al [22]). When a system consists of different components, bodies, or substructures, that are rigid and flexible bodies that are kinematically connected (constrained) by different types of joints, then it is termed a multibody system. Railroad vehicles, automobiles, human bodies, robots, and combustion can be modeled by MBS. In multibody systems, different types of joints are used to kinematically constrain the subsystem motions, which usually subjected to large rotational and translational displacements (Shabana [23]).

In the area of rail, MBS analysis is commonly used for modeling the railroad vehicles and the wheel/rail contact (Shabana et al [24], Shabana and Sany [25]). Coupling FE and MBS has become a procedure that many researchers use to build more complete models in which the two systems linked together and modeled more realistically.

Tanabe et al [26] studied the dynamic interaction of a high-speed train and railway structure under earthquake conditions using a coupled MBS and FE approach. The study included the post-derailment behavior. Another coupled model was created by Galvin et al [27], where a full 3D model was built to analyze the dynamic interaction of high-speed trains with the track and substructure. They used MBS for modeling the vehicle and FEM for modeling the track, while a homogenous half-space model is used for the soil using the boundary element method (BEM).

Ambrosio et al [28] provided a method of coupling multibody systems and finite element codes using independent dynamic integration algorithms. This methodology was tested on a pantograph-catenary interaction simulation in which the pantograph was modeled using MBS and the catenary using FEM.

The main goal of this work is to build a detailed model of the rails and substructure (ballast, sub-ballast, and sub-grade) which couples the FEM with a MBS code for the dynamic analysis in the frequency domain to investigate the effect of the deformable substructure on the deformation of the rail due to the moving vehicle. This coupling will leverage the capabilities of both methods. For instance, the MBS is more efficient for modeling the wheel/rail contact problem, while the FEM is more efficient for modeling the elasticity of the sleepers and the soil layers. Many investigations in the literature use only FEM or MBS for studying a specific problem, but the coupled model presented in

this work allows for a variety of scenarios to be captured while providing a more accurate representation of the track-substructure interaction.

In this work, a detailed model of the substructure is presented. The different three layers: ballast, sub-ballast, and sub-grade are modeled with the corresponding mechanical properties and boundary conditions. Usually, the substructure is modeled using distributed springs or as a layer of ballast supported with specified boundary conditions. The combined analysis between the FEM and MBS is performed in the frequency domain to take advantage of the Floating Frame of Reference (FFR) formulation where the mode shapes are used in place of the nodal degrees of freedom to obtain the elastic response of the system. As the rail is the only component in direct contact with the wheels in the MBS, a nodal elimination procedure is performed in this study after applying the modal analysis to provide the MBS code with the rail nodes data, including mode shapes, and stiffness. This elimination technique helps in modeling a complex model including large number of mode shapes.

In the literature, many researchers used numerical solutions for modeling the wheel/rail contact and then couple it with the FE model they used, but in this work, the coupling between the MBS and FE is done using two specialized codes in FE and MBS to apply the coupling.

The remainder of the paper is organized as follows: Section Two includes the FE modeling of the system, and explains the formulations used in the MBS analysis. It also provides the equations governing the contact forces and the system motion. Numerical results are then presented in Section Three where a comparison is made to verify the model. Finally, the conclusions and future work are presented in Section Four.

2 MODELING

Finite element modeling is used in this work to model the rails, sleepers and the substructure. A full 3D model using beam, solid and spring elements is used to model the different parts of the system. The dynamic analysis and the contact between the wheels and the rails are modeled using a MBS code. The following subsections describe the FE model, including dimensions and material properties. In addition, the MBS formulations are explained in detail in the following subsections, where the formulations of the floating frame of reference, the contact formulations, and the equations of motion are presented.

2.1 FE MODEL

One of the most common numerical techniques for solving engineering problems is the finite element method. FEM is a very powerful tool which can be used to save the cost of building and testing many prototypes by creating numerical models to be tested in a variety of situations. The finite element method is used in this work to model the rails, sleepers, and the substructure (ballast, sub-ballast, and sub-grade). Using a commercially available FE software package, both rails and sleepers are modeled using 3D Beam elements, while the three substructure layers (ballast, sub-ballast, and sub-grade) are modeled using solid elements. Spring-damper elements are used to model the fasteners between the rail and the sleepers. The main dimensions and material properties needed for the different components of the model are provided in Table 1.

Table 1. Finite element model data

3 Description	**4** Value	**5** unit	**6** Description	**7** Value	**8** unit
9 Rigid rail length	**10** 40 (on both sides)	**11** m	**12** Sleeper Poisson's ratio (ε_s)	**13** 0.25	
Gauge length	1.5113	m	Sleeper cross section area (A_r)	513.8e-4	m^2
Flexible rail length	6.5	m	Sleeper second moment of inertia, I_{yy}	25735e-8	m^4
Rail stiffness (E_r)	210e9	N/m^2	Sleeper second moment of inertia, I_{yy}	18907e-8	m^4
Rail density (ρ_r)	7700	kg/m^3	Sleeper Timoshenko shear coefficient	0.83	
Rail Poisson's ratio (ε_r)	0.3		Ballast stiffness (E_b)	260e6	N/m^2
Rail cross section area (A_r)	64.5e-4	m^2	Ballast density (ρ_b)	1300	kg/m^3
Rail second moment of inertia, I_{yy}	2010e-8	m^4	Ballast Poisson's ratio (ε_b)	0.3	
Rail second moment of inertia, I_{zz}	326e-8	m^4	Sub-ballast stiffness (E_{sb})	200e6	N/m^2
Rail Timoshenko shear coefficient	0.34		Sub-ballast density (ρ_{sb})	1850	kg/m^3
Sleeper length	2.36	m	Sub-ballast Poisson's ratio (ε_{sb})	0.35	
Gap between sleepers	0.65	m	Sub-grade stiffness (E_{sg})	200e6	N/m^2
Sleeper stiffness (E_s)	64e9	N/m^2	Sub-grade density (ρ_{sg})	1850	kg/m^3
Sleeper density (ρ_s)	2750	kg/m^3	Sub-grade Poisson's ratio (ε_{sg})	0.3	
Pad stiffness coefficient	26.5e7	N/m	Pad damping coefficient	4.6e4	Ns/m

(K_{pad})			(C_{pad})		

In this model, the track is designed to have a rigid section before and after the flexible section. The rigid sections are assumed to have all degrees of freedom constrained while the deformable section of the rail includes both the rails and the substructure beneath them. The substructure is represented with three layers including the ballast, sub-ballast, and sub-grade. As is shown in Figure 1, the deformable rail is connected to the sleepers using spring-damper elements which are connected to the ballast layer. The substructure layers are constrained on both sides in the longitudinal direction, and the bottom of the sub-grade is also constrained. Figure 2shows the dimensions of the three substructure layers.

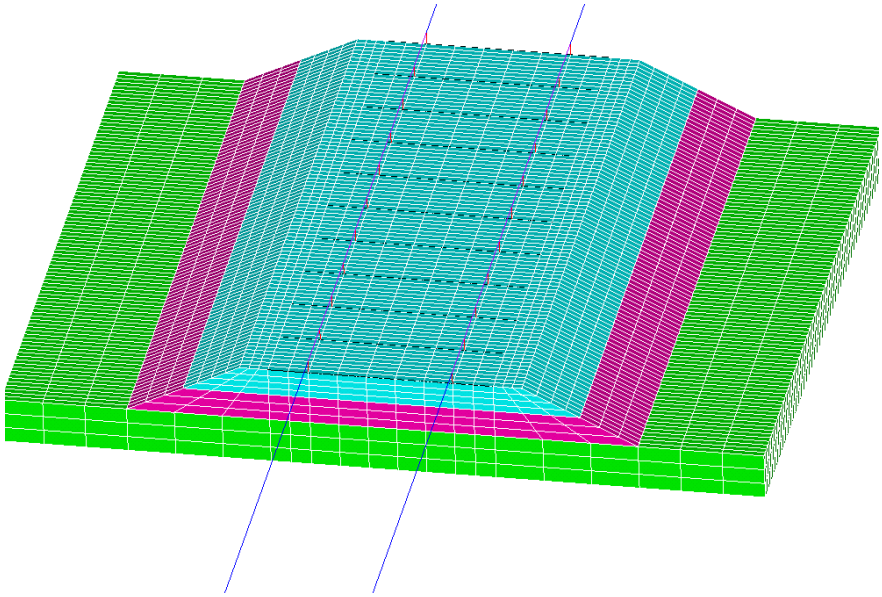

Figure 1. The 3D FE model

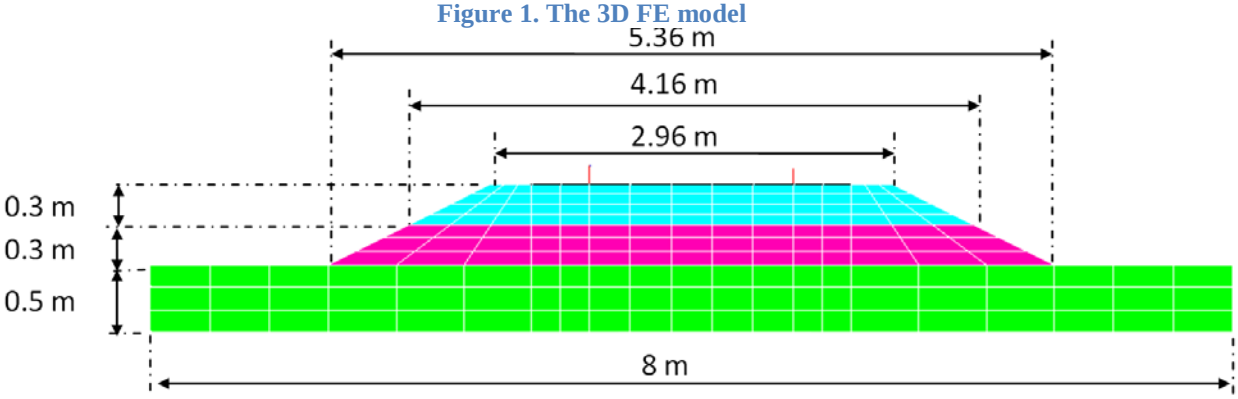

Figure 2. Dimensions of the three substructure layers

Modal analysis was used in this study to obtain the mode shapes and natural frequencies of the FE model, which are used as an input to the MBS code before running the dynamic analysis in the frequency domain. A nodal elimination technique was performed after the modal analysis to provide the MBS code with the mode shapes, modal mass, and stiffness corresponding to only the nodes of the rails. Since only the rail directly interacts with the MBS code, this technique is a successful way to

decrease the size of the arrays in the input file provided to the MBS code and improve efficiency. This reduction in the size of the modal arrays allows for developing much more complicated models with a very large number of nodal degrees of freedom prior to the nodal reduction. At the same time, the number of extracted mode shapes can be increased to ensure the coverage of enough modes for the analysis. Since the load is both concentrated and moving, a high number of mode shapes is generally needed. The model is linear, and this make the modal analysis is very suitable method as it is computationally inexpensive.

13.1 FLOATING FRAME OF REFERENCE FORMULATION

In this investigation, the Floating Frame of Reference (FFR) formulation is used to introduce body flexibility into the equations of motion. The FFR approach takes advantage of the component-mode representation of a Finite Element model, where model is reduced to a set of desired mode shapes, to decrease the system number of degrees of freedom. This reduced model can be then used to evaluate the deformation of flexible bodies in the MBS environment. FFR is ideal for the case of small deformations, such as the case of typical rail deformation, and is also generalized to allow for large rotations. FFR has been applied to modeling rail flexibility in Shabana et al. [29] and been verified by Rathod et al. [30]. In these works, it is shown how the deformation of the rails is taken into account for the prediction of contact points, normal forces, and creepages. A detailed account of the contact prediction and evaluation method is provided in Section 2.2.

Each rail in the track model used is represented by two interdependent models: the geometric model which describes the surface of the rail in the contact prediction algorithm, and the FE model which accounts for the elastic properties of the rail. The rail geometric model as shown in Figure 3 is defined by the following equation:

$$\mathbf{r}^r = \mathbf{R}^r + \mathbf{A}^r\left(\overline{\mathbf{R}}^{rp} + \mathbf{A}^{rp}\overline{\overline{\mathbf{u}}}^{rp}\right) \tag{1}$$

where $\mathbf{r}^r$ defines the position of an arbitrary point on the rail surface, $\mathbf{R}^r$ defines the location of the track coordinate system with respect to the global coordinate system, $\overline{\mathbf{R}}^{rp}$ defines the location of the rail profile coordinate system with respect to the track coordinate system, $\mathbf{A}^{rp}$ defines the orientation of the profile coordinate system with respect to the track coordinate system, and $\overline{\overline{\mathbf{u}}}^{rp}$ defines a point on the rail surface in the profile frame. $\overline{\overline{\mathbf{u}}}^{rp}$ is assumed to be defined by a profile curve describing the contact surface of the rail which is swept along the rail space curve to form a contact surface.

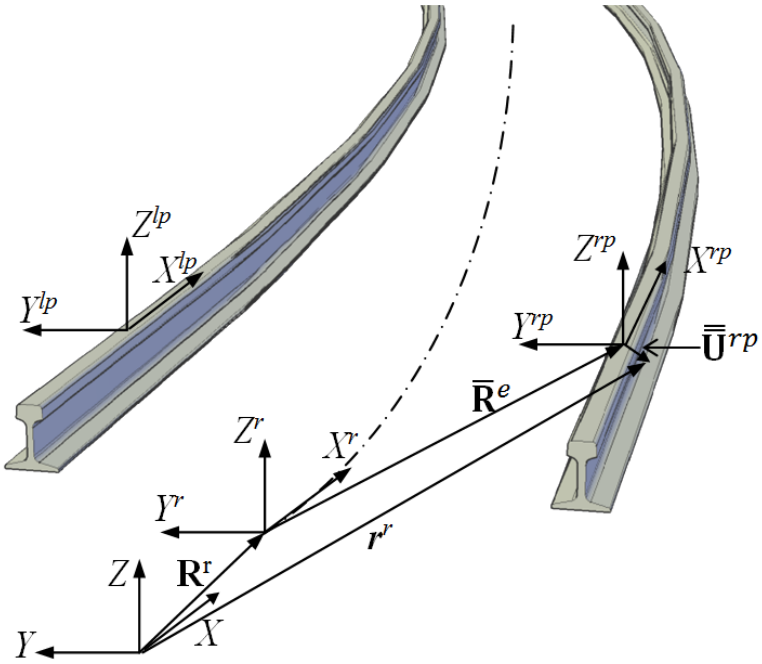

Figure 3. Definition of reference frame

The rail space curve is defined by a series of *Absolute Nodal Coordinate Formulation* (ANCF) 3D beam elements as described in Shabana [31] and may be represented by the following equation:

$$\bar{\mathbf{R}}^{rp}\left(x^r, y^r, z^r, t\right) = \mathbf{S}\left(x^r, y^r, z^r\right)\mathbf{e}^r(t) \tag{2}$$

where $\mathbf{S}$ is the matrix of shape functions for the ANCF 3D beam element provided by Shabana [31], $\mathbf{e}^r$ is the time dependent vector of nodal coordinates which describe the position and first order spatial derivatives of the rail space curve, and x^r, y^r, and z^r are the local coordinates defined in the ANCF element coordinate system. The vector $\mathbf{e}^r$ must be continuously updated to account for the deformation of the FE model as prescribed by Shabana et al. [29]. Note that the nodes of the FE model need not coincide with the nodes of the geometric model as shown in Figure 4.

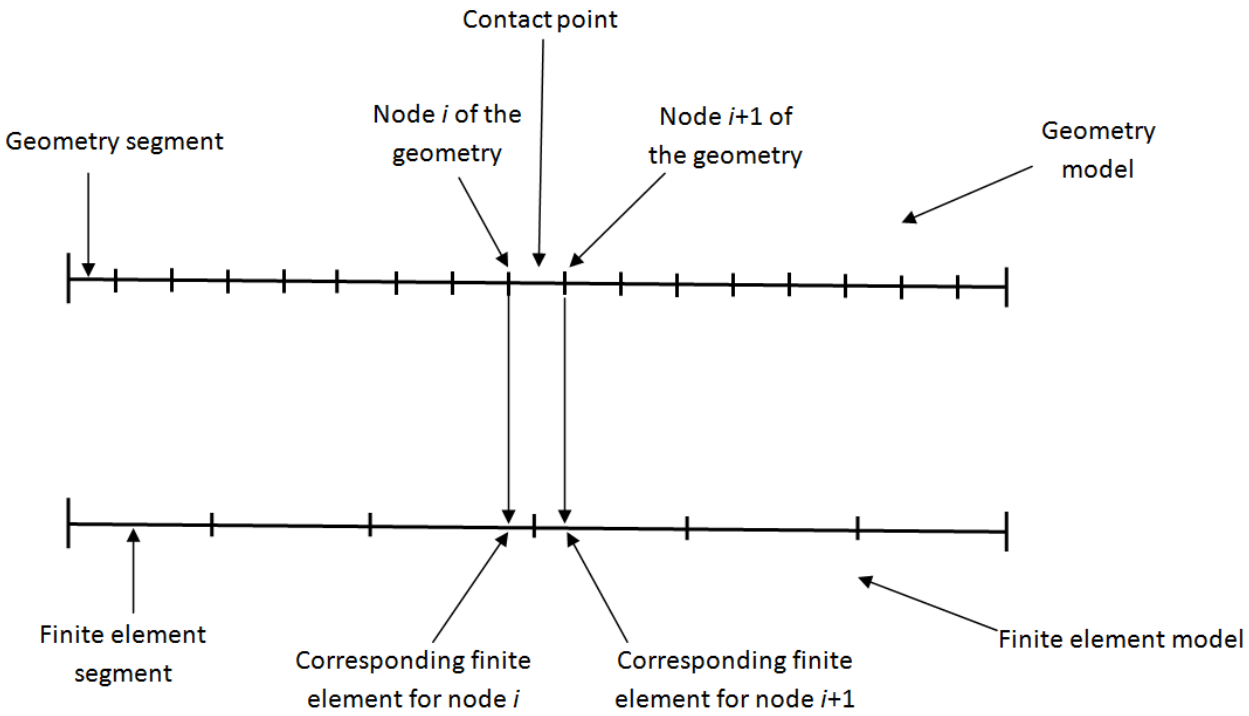

Figure 4. Geometric and finite element nodes

Using the FFR formulation, the FE model of the rail is used to update the ANCF vector of nodal coordinates ($\mathbf{e}^r$). A point on a finite element j in the FE model of rail i may be described with the following equation presented in Shabana [32]:

$$\mathbf{r}^{ij} = \mathbf{R}^i + \mathbf{A}^i\left(\bar{\mathbf{u}}_0^{ij} + \bar{\mathbf{u}}_f^{ij}\right), \quad j = 1,2,...,n_e \tag{3}$$

where $\mathbf{R}^i$ defines the position of the track coordinate system, $\mathbf{A}^i$ defines the orientation of the track body coordinate system with respect to the global coordinate system, n_e is the number of elements in the FE model of rail i. The vectors $\bar{\mathbf{u}}_0^{ij}$ and $\bar{\mathbf{u}}_f^{ij}$ define the position of the point in the reference and deformed configurations respectively and are defined as:

$$\bar{\mathbf{u}}_0^{ij} = \mathbf{S}_b^{ij}\mathbf{B}_c^{ij}\mathbf{e}_{bo}^i, \quad \bar{\mathbf{u}}_f^{ij} = \mathbf{S}_b^{ij}\mathbf{B}_c^{ij}\mathbf{B}_r^i\mathbf{B}_m^i\mathbf{q}_f^i \tag{4}$$

where $\mathbf{S}_b^{ij}$ is the FE shape function matrix associated with element j, $\mathbf{B}_c^{ij}$ is the Boolean element connectivity matrix, $\mathbf{e}_{bo}^i$ is the vector of FE nodal coordinates in the undeformed configuration, $\mathbf{B}_r^i$ is a matrix of reference conditions used to define the element displacement field, $\mathbf{B}_m^i$ is the modal matrix obtained from the FE model which has columns defined by the modes of vibration selected for the analysis, and $\mathbf{q}_f^i$ is the vector of modal coordinates which represent the elastic degrees of freedom in the equations of motion.

13.2 CONTACT FORMULATION

In this investigation, the *Elastic Contact Formulation for Algebraic Equations* (ECFA), presented in Shabana et al [2], is used to predict the location of the contact point. This three-dimensional non-conformal contact approach does not treat the governing equations as constraints, which allows the wheel to have six degrees of freedom with respect to the rail. Small wheel/rail separation and penetration are permitted in ECFA.

Each contact surface is represented in terms of two non-generalized coordinates referred to as surface parameters. This representation allows the location of any point on a contact surfaced to be defined by only two independent coordinates, which greatly simplifies the contact problem. Using this surface parameterization, the following four equations provided by Shabana et al [2] are solved iteratively to determine the location of the contact point for a given wheel and rail pair:

$$\mathbf{E}(\mathbf{s}) = \begin{bmatrix} \mathbf{t}_1^r \cdot \mathbf{r}^{wr} & \mathbf{t}_2^r \cdot \mathbf{r}^{wr} & \mathbf{t}_1^w \cdot \mathbf{n}^r & \mathbf{t}_2^w \cdot \mathbf{n}^r \end{bmatrix}^T = \mathbf{0} \tag{5}$$

where $\mathbf{t}_i^j$ is the tangent vector of surface j taken with respect to surface parameter i, $\mathbf{r}^{wr}$ is defined as the relative difference in position of the contact point on the wheel with respect to the corresponding point on the rail, and $\mathbf{n}^r$ is the normal vector of the rail at the contact point. With the set of surface parameters corresponding to the solution of this equation, the penetration between the wheel and rail must be checked to determine if the solution represents contact or a small separation. The penetration is computed as $\delta = \mathbf{r}^{wr} \cdot \mathbf{n}^r$, where a negative penetration implies contact, and positive penetration implies separation. If the penetration proves that a contact point exists between a given wheel/rail pair, the normal force is computed as $F^N = -K_H \delta^{3/2} - C\dot{\delta}|\delta|$, where $\mathrm{K_H}$ is the Hertzian constant, C is the damping constant, and $\dot{\delta}$ is the time derivative of the wheel/rail penetration. The normal contact force, the location and dimensions of the Hertzian contact ellipse, and the tangential and spin creepages are computed according to the procedure outlined by Shabana et al [2]. Subsequently this data is used to compute the tangential creep forces and the creep spin moment as prescribed by Kalker's non-linear creep theory as described by Shabana et al. [2].

In order to account for the effect of the deformation of the rail on the prediction of the contact point, one must first determine which element in the rail model is in contact with the wheel. Following this, the geometry of the rail is updated and used in the computation of the location and dimensions of the Hertzian contact ellipse as well as the tangential and spin creepages as defined by Kalker [33]. The geometry is updated continuously throughout the iterative procedure used to determine the location of the contact point and the associated forces.

13.3 EQUATIONS OF MOTION

In this investigation, the Augmented Form of the equations of motion presented by Shabana et al., 2005 [23] is implemented. The Augmented Form of the equations of motion is a constrained approach to the solution of the equations of motion in which a system of differential and nonlinear algebraic constraint equations are solved simultaneously. The Augmented Form of the equations of motion may be written as follows [23]:

$$\begin{bmatrix} \mathbf{m}_{rr} & \mathbf{m}_{rf} \\ \mathbf{m}_{fr} & \mathbf{m}_{ff} \end{bmatrix} \begin{bmatrix} \ddot{\mathbf{q}}_r \\ \ddot{\mathbf{q}}_f \end{bmatrix} = \begin{bmatrix} (\mathbf{Q}_e)_r \\ (\mathbf{Q}_e)_f \end{bmatrix} + \begin{bmatrix} (\mathbf{Q}_v)_r \\ (\mathbf{Q}_v)_f \end{bmatrix} - \begin{bmatrix} \mathbf{C}_{\mathbf{q}_r}^T \\ \mathbf{C}_{\mathbf{q}_f}^T \end{bmatrix} \boldsymbol{\lambda} - \begin{bmatrix} \mathbf{0} \\ \mathbf{K}_{ff} \mathbf{q}_f \end{bmatrix} \tag{6}$$

where $\mathbf{m}_{rr}$ is the inertia matrix related to the reference coordinates, $\mathbf{m}_{rf}$ and $\mathbf{m}_{fr}$ are inertia matrices which correspond to the dynamic coupling of the elastic and reference coordinates, $\mathbf{m}_{ff}$ is the inertia matrix related to the elastic coordinates, $\mathbf{q}_r$ is the vector of the generalized rigid body coordinates, $\mathbf{q}_f$ is the vector of elastic modal coordinates of FFR which describe the track and substructure flexibility, $(\mathbf{Q}_e)_r$ and $(\mathbf{Q}_e)_f$ are the vectors of the generalized external forces associated with the rigid and elastic coordinates respectively, $(\mathbf{Q}_v)_r$ and $(\mathbf{Q}_v)_f$ are the vectors of quadratic velocity inertia forces related to the rigid and elastic coordinates respectively, $\mathbf{C}_{\mathbf{q}_r}$ and $\mathbf{C}_{\mathbf{q}_f}$ are the constraint Jacobian matrices related to the rigid and elastic coordinates respectively, $\boldsymbol{\lambda}$ is the vector of Lagrange multipliers, and $\mathbf{K}_{ff}$ is the track stiffness matrix.

The equations of motion are solved for the generalized accelerations and the Lagrange multipliers. Following this solution, the independent coordinates and velocities are found using the explicit Adams-Bashforth-Moulton predictor-corrector numerical integration scheme, as described in Shampine and Gordon [34]. Subsequently, the dependent coordinates and velocities are computed and used to produce the Augmented Form of the equations for the following time step. This procedure continues until such a time that the final time step is completed.

14 NUMERICAL EXAMPLES

The model created in this work is full three dimensional and all the various components are presented as described in Section 2. The model will be used later for more complex problems. Therefore, the verification of the model should be demonstrated. To this end, Recuero's model [9] is compared with the model produced in this investigation. The model used in Recuero's work, which is illustrated in Figure 5, uses beam elements for the rails and sleepers, while the substructure is represented by series of springs under the sleepers. The model created in this investigation, which is illustrated in Figure 6, includes three substructure layers modeled using 8 node solid elements with fasteners modeled using spring-damper elements.

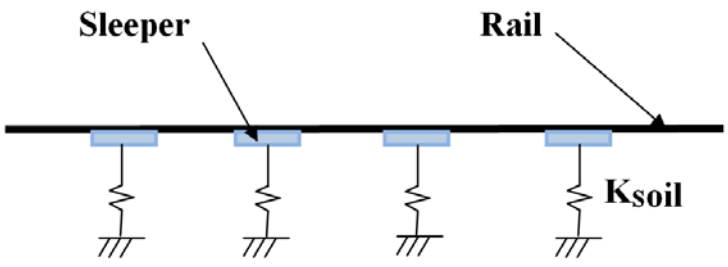

Figure 5. An illustration of Recuero's model [9]

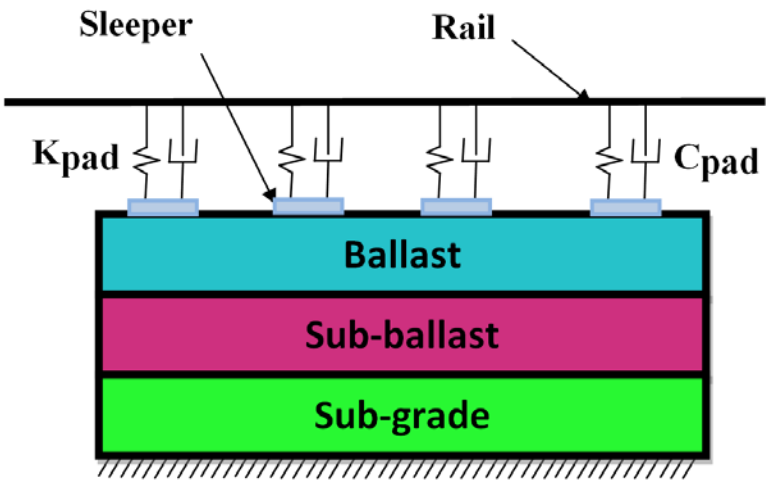

Figure 6. An illustration of the current FE model

The dynamic analysis was performed using MBS code SAMS/2000 [35]. As mentioned above, the MBS code is provided information by the FE model such as mode shapes, modal matrix, mass matrix, and stiffness matrix. The suspended wheelset shown in Figure 7 was used for the dynamic analysis.

We run two examples. The first compares the two models with all the sleepers included while in the second the middle sleeper is unsupported. It is important to note that the spring elements beneath the middle sleeper are removed in both models to model the unsupported case.

Before comparing the results from the model presented in this work and Recuero's model, it was important to check that a sufficient number of nodes were included. A convergence test on the total number of modes was performed for this purpose. A large number of mode shapes were extracted to account for the fact that the applied load to the rail is both very concentrated and moving. Different numbers of mode shapes were used to ensure the convergence as shown in Figure 8. The differences between the peaks are very small, which shows that model is convergence, for example, the difference between the 300 modes case and the 350 modes case is 0.24%. The simulations used in this work are for the case of 300 modes.

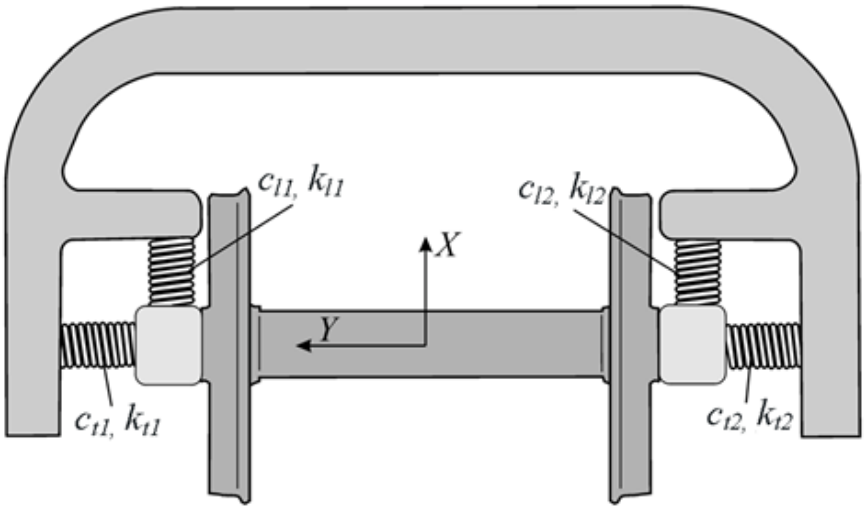

Figure 7. Suspended wheelset used for the dynamic analysis

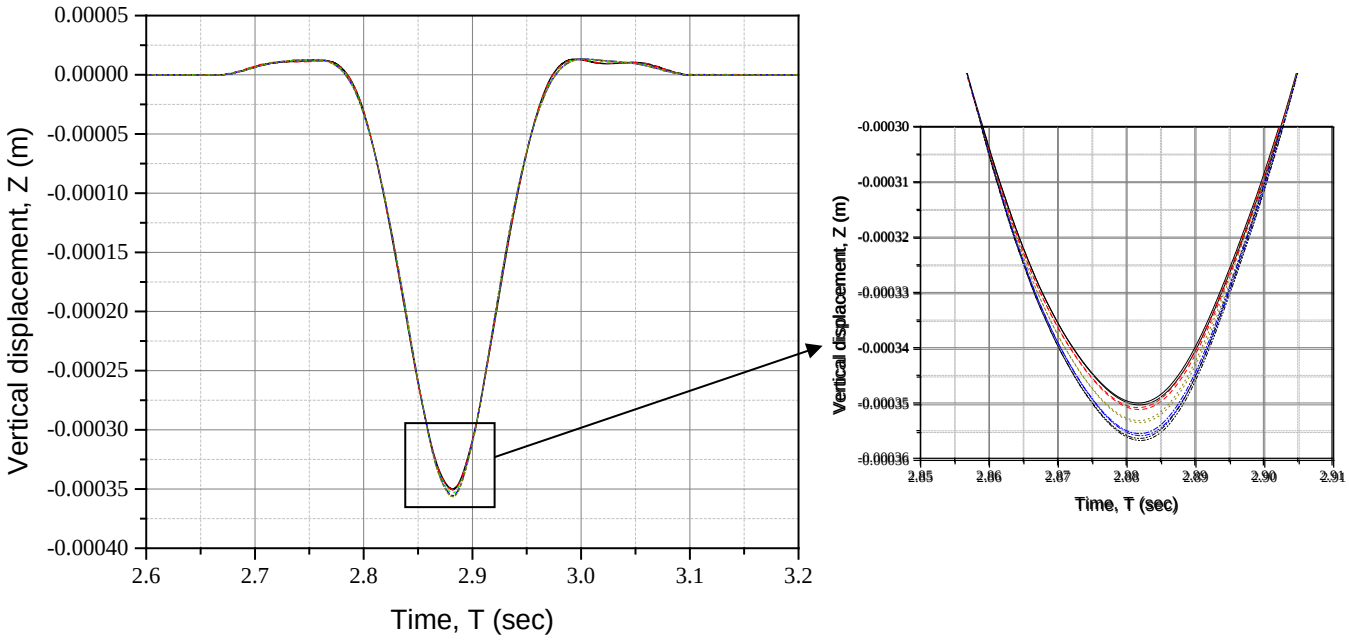

Figure 8. Mode shapes convergence analysis

(150 modes —— , 200 modes - - , 250 modes ···· , 300 modes – , 350 modes - -)

14.1 Supported model

As described previously, the model includes two rigid sections with a deformable section located between them. The deformable section includes 11 supported sleepers. In this section, the vertical displacement (deformation) of the rail is studied at three longitudinal locations along the track. The three positions are: the third sleeper, as shown in Figure 9, the center of the fourth span (between the fourth and fifth sleepers) as shown in Figure 10, and at the middle of the deformable section (the sixth sleeper), as shown in Figure 11.

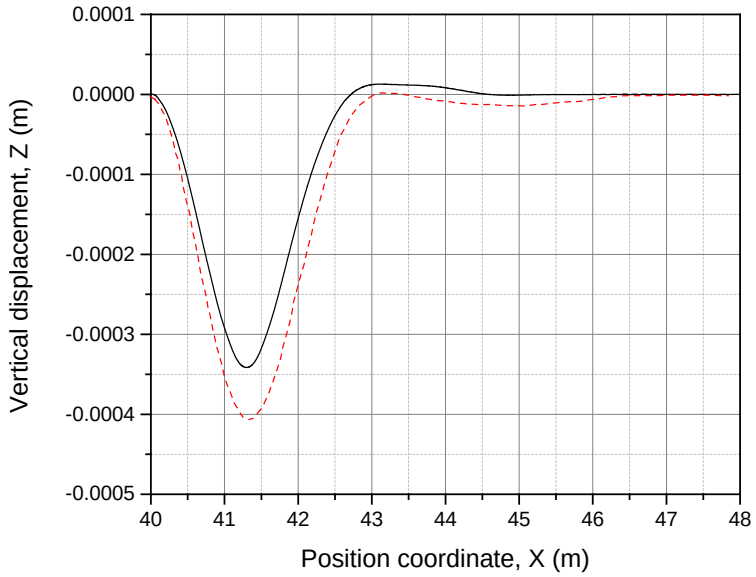

Figure 9. Vertical displacement of the rail at the third sleeper when the wheel/rail contact is directly above it
(Current model ——— , Recuero's model - - - - -)

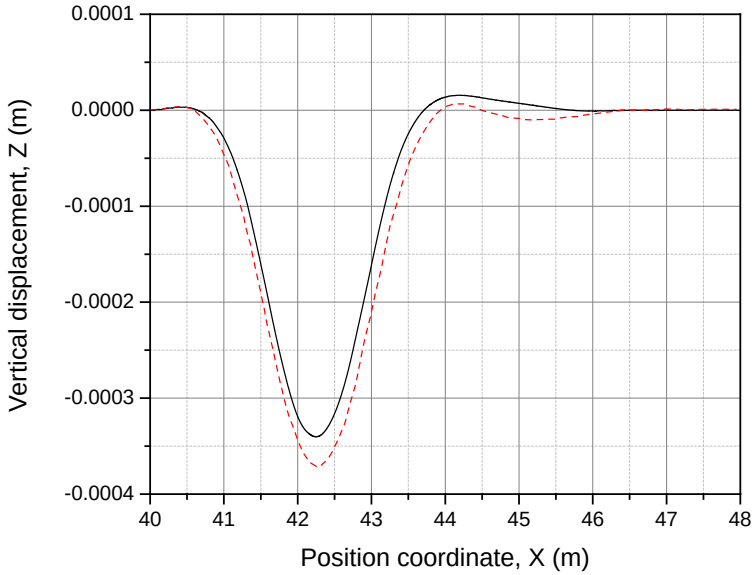

Figure 10. Vertical displacement of the rail at the center of the fourth span when the wheel/rail contact is directly above it
(Current model ——— , Recuero's model - - - - -)

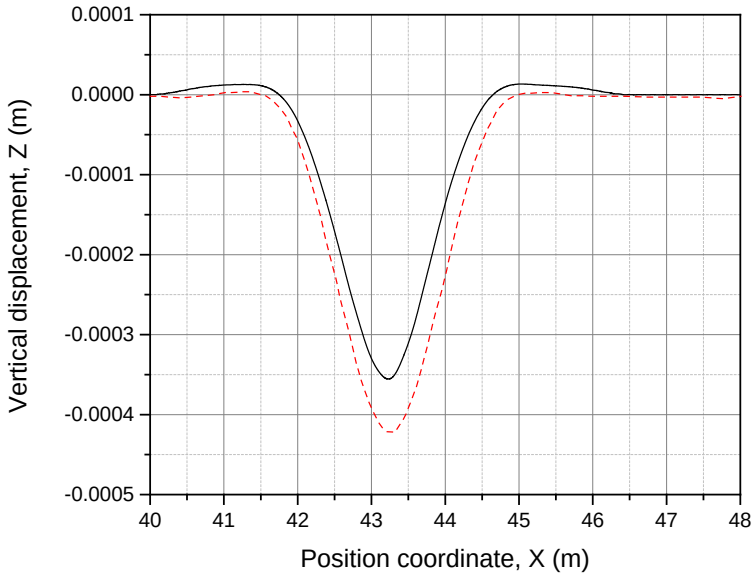

Figure 11. Vertical displacement of the rail at the sixth sleeper when the wheel/rail contact is directly above it
(Current model ——— , Recuero's model - - - - -)

The results show that the two models have the same trend at the three positions, with some difference in the peak values. Some difference is expected as a result of the differences in the models assumptions, for example, the effect of the three layers , and the complexity of the presented FE model compared to the model in the literature. In particular, the Poisson effects in the soil create a slight elevation of the rail on either side of the area of the maximum depression. A model using uncoupled springs for substructure does not capture this phenomenon as well.

14.2 Unsupported rail

In this section, the support of the sleeper in the middle of the deformable rail, sleeper number 6, is removed. In Recuero's model the springs underneath the rail at that position are removed, while in the model presented in this work the fasteners between the rail and the sixth sleeper are removed. The vertical displacements are compared for the two models in the same three positions mentioned in Section 3.1. Figures 12 through 14 show the same performance of the supported rail case.

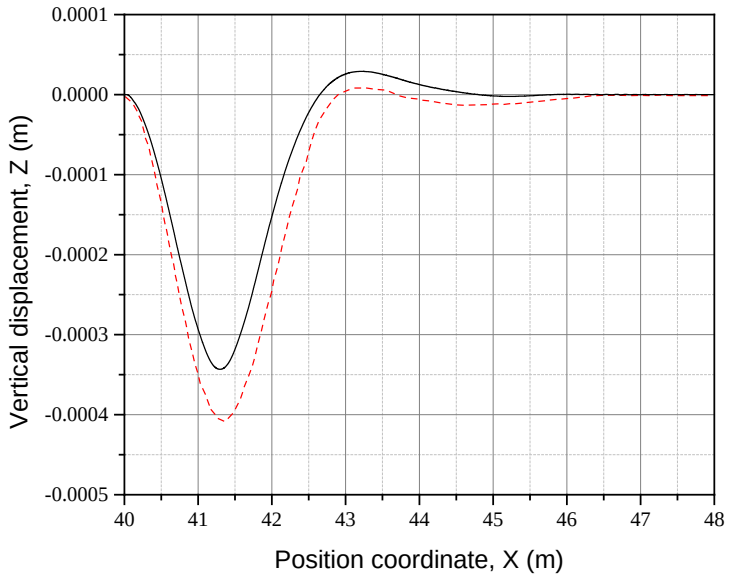

Figure 12. Vertical displacement of the rail at the third sleeper when the wheel/rail contact is directly above it, unsupported middle sleeper

(Current model ——— , Recuero's model - - - - -)

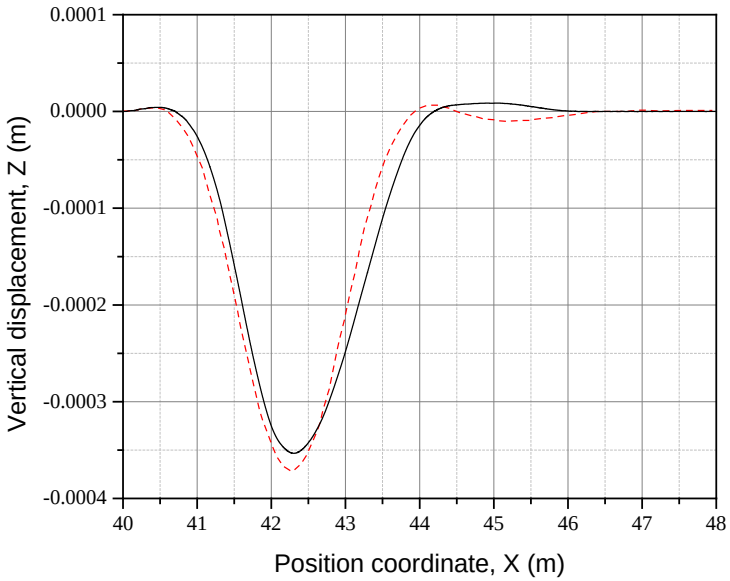

Figure 13. Vertical displacement of the rail at the center of the fourth span when the wheel/rail contact is directly above it, unsupported middle sleeper

(Current model ——— , Recuero's model - - - - -)

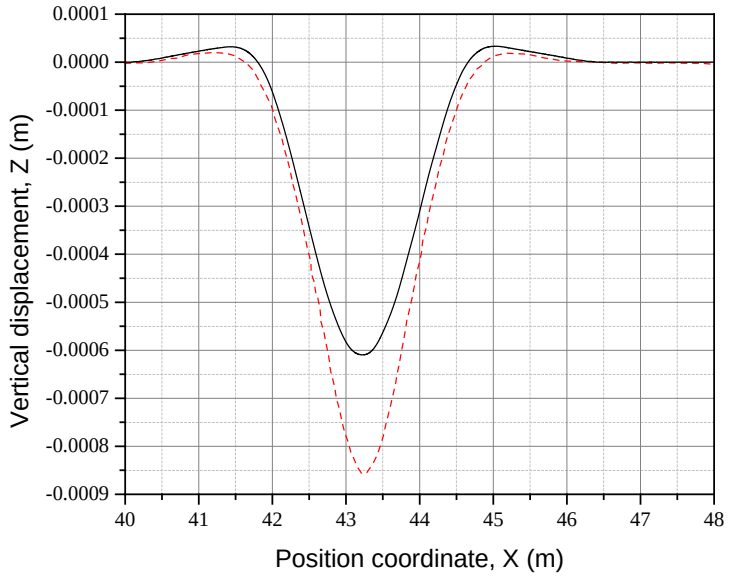

Figure 14. Vertical displacement of the rail at the sixth sleeper when the wheel/rail contact is directly above it, unsupported middle sleeper

(Current model ——— , Recuero's model - - - - -)

The results through the figures show that the presented model has good agreement with the literature. The trend is the same in both cases, and the differences between the peaks are acceptable. The difference between the two models can be explained by the fact that the model in this work includes a much more detailed description of the track substructures than Recuero's model. As in Section 3.1, a similar rise in the rails outside the area of depression is observed.

The results in Sections 3.1 and 3.2 show reasonable agreement with the literature. The figures show the agreement is better in when the comparison is at the center of span between two sleepers than at the sleepers. This difference is due to the fact that the both models have no support at these points, while the support underneath the sleepers is modeled differently in the two models.

15 CONCLUSION

A full 3D full finite element model was created to model the rails, sleepers, and the substructure layers. Beam elements were used to model the rail and sleepers. The model also includes three continuum layers: ballast, sub-ballast, and sub-grade. Each layer was modeled with its own mechanical properties and dimensions. The FE model was linearly coupled with a MBS code in the frequency domain, to provide the dynamic analysis. The work used an elimination technique to reduce the mode shapes provided to the MBS code which enabled the use of a large number of mode shapes. This approach also permits the modeling of an arbitrary complex substructure profile at little additional cost. Verification work was performed by comparing the model output with the literature. The results show good agreement between the FE model and the literature for the two cases presented in the paper. There is some evidence that a continuum model may provide more accurate results than a simple

spring-damper model of substructure, in that there is a rise in the ballast outside the area of depression in the simulation suggestive of Poisson effects.

16 ACKNOWLEDGEMENT

This work was supported by the National University Rail Center (NURail), a US Department of Transportation/ Research and Innovative Technology Administration University Transportation Center. We gratefully acknowledge this support.

17 REFERENCES

1 American Railway Engineering and Maintenance-of-Way Association. (2009). *Manual for railway engineering*. American Railway Engineering and Maintenance-of-Way Association.

2 Shabana, A. A., Zaazaa, K. E., & Sugiyama, H. (2007). *Railroad vehicle dynamics: A computational approach (*Taylor & Francis/CRC, Boca Raton, FL*).*

3 Barbosa, R. S. (2004). A 3D contact force safety crite*rion for flange climb derailment of a railway wheel*. *Vehicle System Dynamics*, *42*(5), 289-*3*00.

4 Sato, Y., Matsumoto, A., Ohno, H., Oka, Y., & Ogawa, *H. (2008). Wheel/rail contact analysis of tramways* a*nd LRVs against derailm*ent. *Wear*, *265*(9), 1460-1464.

5 Wang, W., & Li, G. (2012). Development of high-speed railway vehicle derailment simulation – part II: Exploring the derailment mechanism. *Engineering Failure analysis* 24 (0): 93-111.

6 Huang, H., & Tutumluer, E. (2011). Discrete Element Modeling for fouled railroad ballast. *Construction and Building Materials*, *25*(8), 3306-3312.

7 Brown, S. F., Kwan, J., & Thom, N. H. (2007). Identifying the key parameters that influence geogrid reinforcement of railway ballast. *Geotextiles and Geomembranes*, *25*(6), 326-335.

8 Zhang, S., Xiao, X., Wen, Z., & Jin, X. (2008). Effect of unsupported sleepers on wheel/rail normal load. *Soil Dynamics and Earthquake Engineering*, *28*(8), 662-673.

9 Recuero, A. M., Escalona, J. L., & Shabana, A. A. (2011). Finite-element analysis of unsupported sleepers using three-dimensional wheel–rail contact formulation. *Proceedings of the Institution of Mechanical Engineers, Part K: Journal of Multi-body Dynamics*, *225*(2), 153-165.

10 Lundqvist, A., & Dahlberg, T. (2005). Load impact on railway track due to unsupported sleepers. *Proceedings of the Institution of Mechanical Engineers, Part F: Journal of Rail and Rapid Transit*, *219*(2), 67-77.

11 Sladkowski, A., & Sitarz, M. (2005). Analysis of wheel–rail interaction using FE software. *Wear*, *258*(7), 1217-1223.

12 Monfared , V. (2012). Contact Stress Analysis in Rolling Bodies by Finite Element Method (FEM) Statically. Journal of Mechanical Engineering and Automation 2(2), 12-16.

13 Arslan, M. A., Kayabaşı, O. (2012). 3-D Rail-wheel contact analysis using FEA. *Journal of Advances in Engineering Software* 45(1), 325-331.

14 Xiao, X. B., Wen, Z. F., Jin, X. S., & Sheng, X. Z. (2007). Effects of track support failures on dynamic response of high speed tracks. *International Journal of Nonlinear Sciences and Numerical simulation*, *8*(4), 615-630.

15 Xiao, X., Jin, X., Deng, Y., & Zhou, Z. (2008). Effect of curved track support failure on vehicle derailment. *Vehicle System Dynamics*, *46*(11), 1029-1059.

16 Kumaran, G., Menon, D., & Krishnan Nair, K. (2003). Dynamic studies of railtrack sleepers in a track structure system. *Journal of sound and vibration*, *268*(3), 485-501.
17 Chebli, H., Clouteau, D., & Schmitt, L. (2008). Dynamic response of high-speed ballasted railway tracks: 3D periodic model and in situ measurements. *Soil Dynamics and Earthquake Engineering*, *28*(2), 118-131.
18 Koskinen, M., (2005). Modeling of Soil-Structure Interaction between Railway Bridge and Soil. ABAQUS Users' Conference.
19 Tutumluer, E. (2007). *Discrete element modeling of railroad ballast settlement* (Doctoral dissertation, University of Illinois).
20 Busch, M., & Schweizer, B. (2011). Coupled simulation of multibody and finite element systems: an efficient and robust semi-implicit coupling approach. *Archive of Applied Mechanics*, 1-19.
21 Ibrahimbegović, A., Mamouri, S., Taylor, R. L., & Chen, A. J. (2000). Finite element method in dynamics of flexible multibody systems: modeling of holonomic constraints and energy conserving integration schemes. *Multibody System Dynamics*, *4*(2), 195-223.
22 Heege, A., Betran, J., & Radovcic, Y. (2007). Fatigue load computation of wind turbine gearboxes by coupled finite element, multi-body system and aerodynamic analysis. *Wind* Energy, 10(5), 395-413.
23 Shabana, A. A. (2005). Dynamics of multibody systems. Cambridge University Press.
24 Shabana, A. A., Tobaa, M., Sugiyama, H., & Zaazaa, K. E. (2005). On the computer for*mulations o*f *th*e wheel/rail contact problem. *Nonlinear Dynamics, 40(2), 169*-193.
25 Shabana, A. A., & Sany, J. R. (2001). A survey of rail vehicle track simulations and flexible multibody dynamics. *Nonlinear Dynamics*, *26*(2), 179-212.
26 Tanabe, M., Wakui, H., Sogabe, M., Matsumoto, N., & Tanabe, Y. (2010). A combined multibody and finite element approach for dynamic interaction analysis of high-speed train and railway structure including post-derailment behavior during an earthquake. In *IOP Conference Series: Materials Science and Engineering* (Vol. 10, No. 1, p. 012144). IOP Publishing.
27 Galvín, P., Romero, A., & Domínguez, J. (2010). Fully three-dimensional analysis of high-speed train–track–soil-structure dynamic interaction. *Journal of Sound and Vibration*, *329*(24), 5147-5163.
28 Ambrósio, J., Pombo, J., Rauter, F., & Pereira, M. (2008). A memory based communication in the co-simulation of multibody and finite element codes for pantograph-catenary interaction simulation. *Multibody Dynamics*, 231-252.
29 Shabana, A.A., Chamorro, R and Rathod, C., 2007. "A Multibody System Approach for Finite-Element Modeling of Rail Flexibility in Railroad Vehicle Applications". *J. Multi-body Dynamics*, Vol. 222 Part K, 1-15.
30 Rathod, C., Chamorro, R., Escalona, J.L., El-Sibaie, M. and Shabana, A.A., 2009 "Validation of a Three-Dimensional Multibody System Approach for Modeling Track Flexibility". *J. Multi-body Dynamics*, Vol. 223 Part K, 269-281.
31 Shabana, A. A., 2012. *Computational Continuum Mechanics*. Cambridge: Second Edition, Cambridge UP, 2012.
32 Shabana, A.A., 2005. *Dynamics of Multibody Systems*, 3rd edition, Cambridge University Press, Cambridge, UK.
33 Kalker, J. J. *Three-dimensional elastic bodies in rolling contact*, 1990 (Kluwer, Dordrecht).
34 Shampine, L.F., and Gordon, M.K., 1975. *Computer Solution of Ordinary Differential Equations: The Initial Value Problem*. W.H. Freeman, San Francisco, USA.

35 Shabana, A. A., 2010. *Computational Dynamics*, 3rd ed., John Wiley & Sons, Chichester, West Sussex.

National University Rail Center - NURail
US DOT OST-R Tier 1 University Transportation Center

NURail Project ID: NURail2012-UIC-R01-B

Modeling of Rail Track Substructure
Soil Plasticity Modeling

By

Craig Foster
Associate Professor
Departmet of Civil and Materials Engineering
University of Illinois at Chicago
fosterc@uic.edu

Mohammad Hosein Motamedi
Graduate Research Assistant
Department of Civil and Materials Engineering
University of Illinois at Chicago
mmotam2@uic.edu

30-09-2015

Grant Number: DTRT12-G-UTC18

DISCLAIMER

Funding for this research was provided by the NURail Center, University of Illinois at Urbana - Champaign under Grant No. DTRT12-G-UTC18 of the U.S. Department of Transportation, Office of the Assistant Secretary for Research & Technology (OST-R), University Transportation Centers Program. The contents of this report reflect the views of the authors, who are responsible for the facts and the accuracy of the information presented herein. This document is disseminated under the sponsorship of the U.S. Department of Transportation's University Transportation Centers Program, in the interest of information exchange. The U.S. Government assumes no liability for the contents or use thereof.

National University Rail Center - NURail
US DOT OST-R Tier 1 University Transportation Center

TECHNICAL SUMMARY

Title

Modeling of Rail Track Substructure – Soil Plasticity Modeling

Introduction

Elastic modeling of soil is unable to unable capture permanent deformation and settlement in soil that may come from rail applications. In addition, elastic models may not correctly predict dynamic deformation of soil. We modify a soil model an elasto-viscoplastic soil model to account for better performance at low mean stresses and improve its numerical implementation.

Approach and Methodology

We modify the Sandia Geomodel, a three-invariant, cap plasticity model with isotropic and kinematic hardening, with a tension cap for more realistic behavior in the tensile regime. We rewrite the yield function in terms of a homogenous function of order one to prevent spurious solutions that troubled previous implementations. Finally, we create an algorithm to determine from the trial state whether we are on the shear or cap surface, enhancing robustness. These are implemented in a fully implicit, unconditionally stable return-mapping algorithm.

Findings

The tension cap creates more realistic behavior for the material in tension. The other improvements enhance both robustness and efficiency of the model. Several examples show that the model can capture many behaviors of soils and rock.

Conclusions

The improved model can better capture, and in a more robust fashion, the behavior of geomaterials for rail and other applications.

Recommendations

For applications of soil settlement, an advanced plasticity model can better account for realistic behavior of the soil and can be employed.

Publications

M. H. Motamedi and C. D. Foster, "An improved implicit numerical integration of a non-associated, three- invariant cap plasticity model with mixed isotropic-kinematic hardening for geomaterials." *International Journal of Numerical and Analytical Methods in Geomechanics.*In press.

Primary Contact

Principal Investigator
Craig D. Foster
Associate Professor
Department of Civil and Materials Engineering
University of Illinois at Chicago
312-996-8086
foster@uic.edu

Other Faculty and Students Involved
Mohammad Hosein Motamedi
Graduate Research Assistant
Department of Civil and Materials Engineering
University of Illinois at Chicago
312-996-0438
mmotam2@uic.edu

NURail Center
217-244-4999
nurail@illinois.edu
http://www.nurailcenter.org/

TABLE OF CONTENTS

TABLES

LIST OF FIGURES

18 INTRODUCTION

Geological materials are broadly utilized in nature and engineering applications. Modeling the behavior of geomaterials has attracted much research effort with the advent of modern computational technology schemes. Particle mechanics models such as the Discrete Element Method (DEM) [1–3] and Lattice Element Method (LEM) [4,5] have been developed to investigate micromechanical features of complex geomaterials. Despite the remarkable insight those models provide, they need significant computational power to realistically achieve engineering scale problems. In order to reduce computational effort, multiscale computational approaches have been developed. These methods are generally classified as either hierarchical or concurrent schemes [6–10]. However, the micromechanically-based evolution of plastic internal variables (PIVs) adopted in these models is nonsmooth. Accurately handling these nonsmooth evolution laws necessitates special treatments which are numerically cumbersome. A work by Tu et al. [11] makes a clear attempt to address this issue. Further, nonsmooth evolution laws may not be integrable using implicit methods and hence necessitate small step sizes for stability. This limitation underscores its deficiency when the model is applied in numerical simulations for some practical cases such as tunneling or excavation in which the load increment could be locally large, and the step size cannot be greatly reduced to achieve required accuracy.

On the other hand, recent studies have revealed numerous complexities in the inelastic behavior and failure mode of geomaterials [12,13]. For instance, sedimentary rocks, including sandstone and limestone, feature a diversity of micromechanical processes and fundamental differences with respect to inelastic compaction. In sandstone, inelastic compaction is most likely associated with an intragranular cracking phenomenon arising from local tensile stress concentration at grain contacts. In limestone, by contrast, pore collapse engendered by stress concentrations at the surface of the pores dominates the compaction processes. A comprehensive review of the different damage processes of porous rocks in both brittle faulting and cataclastic flow has been presented in Ref. [13]. Consequently, micromechanical models, even cast in a multi-scale framework, are unable to integrate the full complexities of geomaterials in a consistent and unified manner with acceptable computational cost.

Elastoplasticity is still the most widely acknowledged method to capture material nonlinearities and inelastic behavior in geomaterials. During the last decade, much research work has been devoted in the framework of elastoplasticity to capture one or more complex, yet crucial, features of geomaterial behavior [14–20]. Recently, Tengattini et al. [20] proposed a thermomechanical-based continuum constitutive model for cemented granular materials. Although the model successfully employed scalar internal variables to describe grain crushing and cement damage process, the authors point out that it is unable to replicate deformation induced anisotropy associated with dilatant failure mode.

Cap plasticity models such as the one originally proposed by DiMaggio and Sandler [21], have occupied a prominent place in continuum geomechanics due to their versatility and ability to capture complex features of geomaterials such as soils, rocks, and concrete [22–27]. For traditional cap models, some difficulties arise from the singularities induced by the nonsmooth intersection of the compression cap and shear surface. While specific algorithms have been developed to handle non-smooth intersections, they often introduce severe algorithmic and numerical complexities [28]. To circumvent this issue, a number of smooth variations of the multisurface plasticity models have been proposed [29–33].

Even though recent advances in the development of three-invariant cap plasticity theory endowed models with improved local predictive capability, they still suffer from difficulties in numerical implementation. In explicit [26, 31] and semi-implicit [36] implementations, the lack of unconditional stability may require very small time steps for large-scale problems. On the other hand, fully implicit schemes [34, 35] can require complex algorithms that are costly at the local level and may suffer from robustness issues.

The Sandia GeoModel is an advanced three-invariant cap plasticity model which has been developed for application to geomaterials [26]. The parameterization procedure has been carried out for many geological materials including frozen soil, limestone, tuff, diatomite, granodiorite, and concrete. To increase computational efficiency, Foster et al. [34] presented an algorithm for the implicit integration of this model in the case of combined isotropic and kinematic hardening using the spectral decomposition of the relative stress. In the aforementioned study, all numerical examples were carried out on a single element using the associative version of the model to illustrate the quadratic convergence of the proposed algorithm. Regueiro and Foster [35] conducted a bifurcation analysis on this three-invariant cap plasticity model to investigate the onset and orientation of strain localization. They again provide a number of numerical examples on a single 3D solid element. Sun et al. [36] adopted this three-invariant cap model coupled with a fluid flow model to simulate the hydro-mechanical interactions of fluid-infiltrating porous rocks. To bypass the numerical difficulties, they employ a refined explicit integration algorithm whose accuracy and stability both depend significantly on the chosen time step size.

In this work, we address the aforementioned potential issues which one may confront with regard to full-scale non-linear finite element simulation using an advanced phenomenological continuum constitutive model. As a result, the Sandia GeoModel yield function and relevant plastic potential are reformulated without a need to change material parameters. This new formula eliminates spurious solutions attributed to original form of the yield function. The smooth elliptical tension cap added to the model extends the domain of applicability to the tensile loading. The model is applied to fully implicit, unconditionally stable time integration algorithm using a return-mapping scheme in principal relative stress (or strain) directions. The yield function reformulation increases computational efficiency for both locally and globally iterative solutions. The novel “a priori shear/cap surface determination” algorithm is introduced to efficiently reduce the computational cost meanwhile the shear yield surface operates in the case of kinematic hardening. Nonassociative models generally provide a more realistic response for low porous geomaterials, particularly with respect to dilation. Hence, the algorithmically consistent elastoplastic modulus is also derived based on nonassociated plasticity flow rule to better describe volumetric material behavior.

19 ELASTO/VISCOPLASTIC CONSTITUTIVE EQUATIONS: RATE SENSITIVE, NONASSOCIATED FLOW RULE WITH MIXED HARDENING

In this section, the continuum constitutive equation is formulated within the framework of infinitesimal elastoplasticity.

19.1 BASIC EQUATIONS

For the infinitesimal strain case, the strain tensor can be approximated by

$$\boldsymbol{\varepsilon} = \nabla^s(\boldsymbol{u}) \coloneqq \frac{1}{2}[\nabla \boldsymbol{u} + (\nabla \boldsymbol{u})^T] \tag{1}$$

where $\boldsymbol{u}$ is the displacement field

The stress rate constitutive equation for linear isotropic elasticity can be written as:

$$\dot{\boldsymbol{\sigma}} = \boldsymbol{C^e} : \dot{\boldsymbol{\varepsilon}}^{\boldsymbol{e}}, \boldsymbol{C^e} = \lambda \mathbf{1} \otimes \mathbf{1} + 2\mu \boldsymbol{I} \tag{2}$$

where $\mathbf{1}$ is the second order identity tensor, $(\mathbf{1})_{ij} = \delta_{ij}$ (δ_{ij} is the Kronecker delta.), $\boldsymbol{I}$ is the fourth-order symmetric identity tensor, $(\boldsymbol{I})_{ijkl} = \frac{\mathbf{1}}{\mathbf{2}}\left(\delta_{ik}\delta_{jl} + \delta_{il}\delta_{jk}\right)$, λ and μ are the Lamé parameters.

2.2. VISCOPLASTICITY EQUATIONS

The hypothesis of small deformations and rotations allows an additive decomposition of the total strain rate $\dot{\varepsilon}$ into the elastic and inelastic parts as below

$$\dot{\boldsymbol{\varepsilon}} = \dot{\boldsymbol{\varepsilon}}^{\boldsymbol{e}} + \dot{\boldsymbol{\varepsilon}}^{\boldsymbol{in}} \tag{3}$$

The inelastic strain $\boldsymbol{\varepsilon^{in}}$ will be denoted as plastic strain $\boldsymbol{\varepsilon^{p}}$ for the classical rate-independent plasticity and viscoplastic strain $\boldsymbol{\varepsilon^{vp}}$ for the rate-dependent material behavior.

The closed convex elastic domain in the stress space is expressed as:

$$E \coloneqq \{\boldsymbol{\sigma} \in \boldsymbol{S} : f(\boldsymbol{\sigma}, \boldsymbol{q}) \leq 0\} \tag{4}$$

$$\partial E \coloneqq \{\boldsymbol{\sigma} \in \boldsymbol{S} : f(\boldsymbol{\sigma}, \boldsymbol{q}) = 0\} \tag{5}$$

where $\boldsymbol{S}$ is stress space and $f(\boldsymbol{\sigma}, \boldsymbol{q})$ denotes the yield function whose zero-level set provides the boundary of the elastic domain. In this work, the evolution of the stress-like plastic internal variables $\boldsymbol{q}$ is characterized in terms of a phenomenological hardening law as below

$$\dot{\boldsymbol{q}} = \dot{\gamma} \boldsymbol{h^q}(\dot{\boldsymbol{\varepsilon}}^{\boldsymbol{p}}, \boldsymbol{q}) \tag{6}$$

Here $\dot{\gamma}$ is the plastic consistency parameter which denotes the magnitude of the plastic flow rate. By using a plastic potential function g, a non-associated plastic flow rule is derived in a form of

$$\dot{\boldsymbol{\varepsilon}}^{\boldsymbol{p}} = \dot{\gamma} \frac{\partial g}{\partial \boldsymbol{\sigma}} \tag{7}$$

The flow rule is associative if the material parameters are chosen such that $f = g$.

In rate form, the consistency condition is utilized to find the non-negative parameter $\dot{\gamma}$

$$\dot{f} = \frac{\partial f}{\partial \boldsymbol{\sigma}} : \dot{\boldsymbol{\sigma}} + \frac{\partial f}{\partial \boldsymbol{q}} : \dot{\boldsymbol{q}} = 0 \tag{8}$$

then solving the equation for $\dot{\gamma}$ concludes to

$$\dot{\gamma} = \frac{1}{\chi} \frac{\partial f}{\partial \boldsymbol{\sigma}} : \boldsymbol{C^e} : \dot{\boldsymbol{\varepsilon}} \tag{9a}$$

in which

$$\chi = \frac{\partial f}{\partial \boldsymbol{\sigma}} : \boldsymbol{C^e} : \frac{\partial g}{\partial \boldsymbol{\sigma}} - \frac{\partial f}{\partial \boldsymbol{q}} : \boldsymbol{h^q} \tag{9b}$$

Eventually, the continuum elasto-plastic tangent $\boldsymbol{C^{ep}}$ can be derived by substituting Eq. (9a) into Eq. (7) and manipulating with Eqs. (2) and (3)

$$\dot{\boldsymbol{\sigma}} = \boldsymbol{C^{ep}} : \dot{\boldsymbol{\varepsilon}};\ \boldsymbol{C^{ep}} = \left(\boldsymbol{C^e} - \frac{1}{\chi} \boldsymbol{C}^e : \frac{\partial g}{\partial \boldsymbol{\sigma}} \otimes \frac{\partial f}{\partial \boldsymbol{\sigma}} : \boldsymbol{C^e}\right) \tag{10}$$

2.3. APPLICATION TO THE MODIFIED VERSION OF SANDIA GEOMODEL

In this section the formulation of a three-invariant, rate-dependent and nonassociative cap plasticity model is described. The model is a modified version of the Sandia GeoModel [26] and comprises a nonlinear shear limit-state surface as well as elliptical compression and tension caps. Fig. 1a shows the 3D representation of the model in the principal stress space. The Gudehus-type model is adopted using the third stress invariant to replicate the strength differential (SD) effect, which is the difference in strength of geomaterials observed in triaxial compression and extension tests. The rounded triangular shape of the model in deviatoric planes is illustrated in Fig. 1b. Triaxial compression *(TXC)* and triaxial extension *(TXE)* denote the two main canonical stress paths.

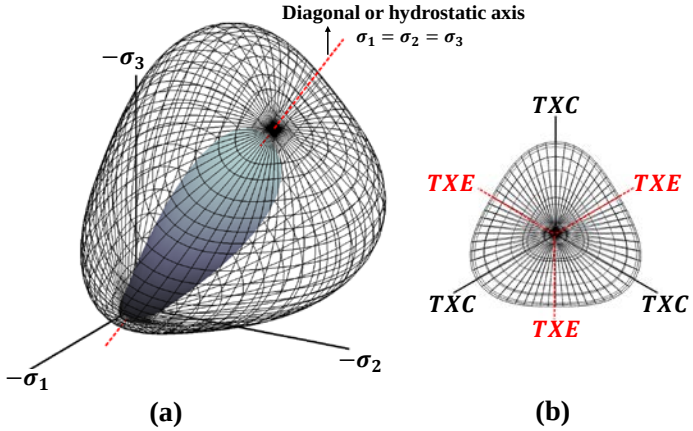

Fig. 1. Cap plasticity model: (a) three dimensional view of the yield surface (the exterior free mesh surface) and plastic potential surface (the interior gray solid) in principal stress space; (b) octahedral view, which corresponds to looking down the hydrostatic axis (lines of triaxial compression (TXC), triaxial extension (TXE) marked).

2.3.1. YIELD FUNCTION AND PLASTIC POTENTIAL

Assuming the yielding behavior is isotropic, the yield function can be expressed in terms of stress invariants. In the case of kinematic hardening, this can be extended to the use of the invariants of the relative stress. The relative stress tensor is defined as $\boldsymbol{\xi} := \boldsymbol{\sigma} - \boldsymbol{\alpha}$ and its three independent invariants are given by

$$I_1 = \mathrm{tr}(\boldsymbol{\xi}) = \mathrm{tr}(\boldsymbol{\sigma}),\ (\ \mathrm{tr}(\boldsymbol{\alpha}) = 0\ ) \tag{11a}$$

$$J_2^{\xi} = \frac{1}{2}\, dev\, \boldsymbol{\xi} : dev\, \boldsymbol{\xi} \tag{11b}$$

$$J_3^{\xi} = \det(dev\, \boldsymbol{\xi}) = \frac{1}{3}\,(dev\, \boldsymbol{\xi} \cdot dev\, \boldsymbol{\xi}) : dev\, \boldsymbol{\xi} \tag{11c}$$

In this study, the yield function f takes the following form:

$$f = \Gamma(\beta^{\xi})\sqrt{J_2^{\xi}} - \sqrt{F_c}\,(F_f - N) \tag{12}$$

where Γ accounts for the difference in triaxial extension vs. compression strength

$$\Gamma(\beta^{\xi}) = \frac{1}{2}\left[1 + \sin(3\beta^{\xi}) + \frac{1}{\psi}\left(1 - \sin(3\beta^{\xi})\right)\right] \tag{13a}$$

in which

$$\beta^{\xi}\left(J_2^{\xi}, J_3^{\xi}\right) = \frac{-1}{3}\sin^{-1}\left(\frac{3\sqrt{3}J_3^{\xi}}{2\left(J_2^{\xi}\right)^{3/2}}\right) \tag{13b}$$

The Lode angle β^{ξ} is a function of the second and third invariants of the deviatoric relative stress $dev\ \boldsymbol{\xi}$. Here, ψ is a material constant which denotes the ratio of triaxial extension strength to compression strength. The strength differential (SD) effect arises from pressure-induced friction on microcrack faces and grain boundaries, which enables the material to withstand higher loads when the most critical surface is under higher compression. The exponential shear failure function F_f captures the pressure dependence of the shear strength of the material.

$$F_f(I_1) = A - C\ exp(\ BI_1\ ) - \theta I_1 \tag{14}$$

where A, B, C and θ are all non-negative material parameters determined from peak stress experimental data, using a procedure described in [26]. The material parameter *N* characterizes the maximum allowed translation of the initial yield surface during kinematic hardening.

As seen in Eq. (12), the simple, yet important, modification is provided in the format of the yield function via individually taking the square root of all terms involved in the formula such that no adjustment is needed in material parameters. This modification is a change to previous versions of the model, which used squared versions of each term on the right-hand side. While the original form tends to be at an advantage in providing simplified yield function derivatives for user friendly FE implementation, it may trigger spurious solutions in solving the nonlinear optimization problem. The optimization problem for modeling of plasticity is accompanied by set of equalities and inequalities, known as the Kuhn-Tucker conditions and derived based on the rules of Lagrange multipliers method [37,38]. In addition, this alternative form enhances computational efficiency and robustness in the framework of iterative integration algorithm. The comparative results will be presented later in Section 4 to underscore the importance of this reformulation.

The cap function F_c , as graphically illustrated in Fig. 2, couples hydrostatic (either tensile or compressive) and deviatoric stress-induced deformation. Unlike the previous forms of the model, which only included the compression cap, the new formula, Eq. 15a, generates smooth elliptical tension and compression caps to the yield function.

$$F_c(I_1, \kappa, T) = 1 - H(\kappa - I_1)\left(\frac{I_1 - \kappa}{X(\kappa) - \kappa}\right)^2 - H(I_1 - I_1^T)\left(\frac{I_1 - I_1^T}{3T - I_1^T}\right)^2 \tag{15a}$$

$$X(\kappa) = \kappa - RF_f(\kappa) \tag{15b}$$

where $H(\bullet)$ is the Heaviside function, κ allocates the branch point where combined porous/microcracked yield surface deviates from the nonporous profile for full dense bodies. X marks the position at which pressure under hydrostatic loading would be sufficient to prompt grain crushing and pore collapse mechanisms. The material parameter R governs the aspect ratio of the compression cap surface.

As illustrated in Fig. 2, I_1^T and T indicate the initiation point of the tension cap and the hydrostatic tensile strength of the material, respectively. A number of standard tension tests have been developed to measure these mechanical parameters [39,40]. This modification makes the model more applicable to the problems (e.g. retaining walls and hill-slopes) in which the stress paths may experience some tension.

Initially, plasticity models included a tension cut-off type surface to account for tensile failure phenomenon. This simplification introduces an additional singularity problem (corner region problem), at the intersection of shear and tension surfaces. As a result, Swan and Seo [32] proposed a model

accompanied with a circular tension cap. This circular meridian section may not be as accurate as elliptical forms whose aspect ratio property allows a better representation of experimental data.

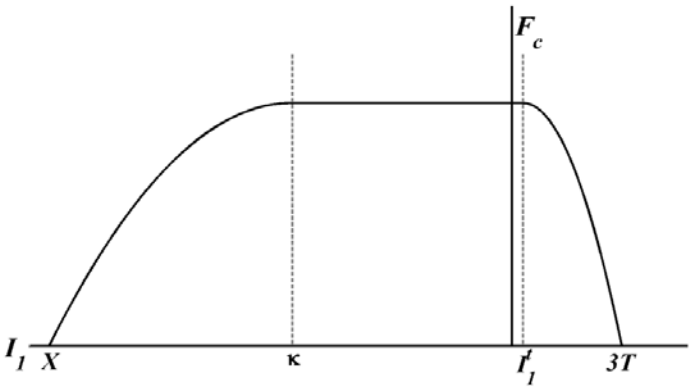

Fig. 2. Cap function F_c

For geomaterials, nonassociated plasticity is usually needed to realistically describe volumetric deformation [41–43]. As pointed out by McDowel [44], nonassociativity in geological materials can be described with structural rearrangement. This physical phenomenon has been observed in conjunction with growth of microcracks, propagation of shear bands and pressure dependence of frictional shear resistance. Hence, similar to the yield function, but with different material parameters, plastic potential g is presented in Eq. (16) and illustrated in Figs. 1a and 3.

$$g = \Gamma^{\xi}(\beta^{\xi})\sqrt{J_2^{\xi}} - \sqrt{F_c^{g}}\,(F_f^{g} - N) \tag{16}$$

in which

$$F_f^{g}(I_1) = A - C\,exp(\,LI_1\,) - \varphi I_1 \tag{17a}$$

$$F_c^{g}(I_1, \kappa, T) = 1 - H(\kappa - I_1)\left(\frac{I_1 - \kappa}{X^{g}(\kappa) - \kappa}\right)^2 - H(I_1 - I_1^{T})\left(\frac{I_1 - I_1^{T}}{3T - I_1^{T}}\right)^2 \tag{17b}$$

$$X^{g}(\kappa) = \kappa - QF_f^{g}(\kappa) \tag{17c}$$

where Q is a material parameter analogous to R.

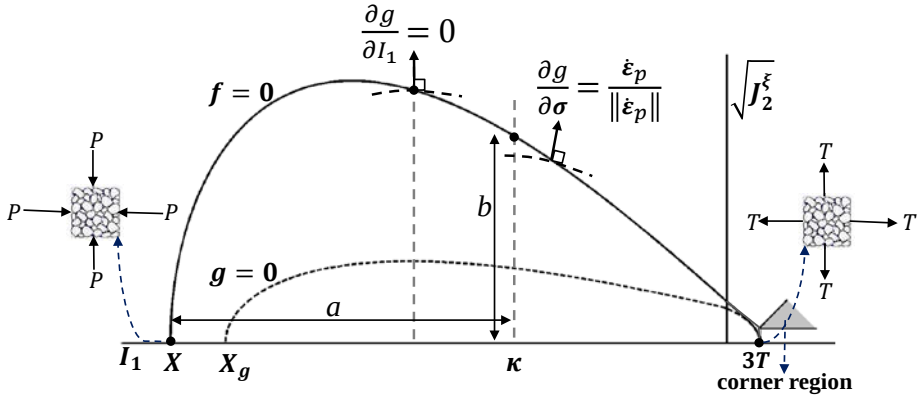

Fig. 3. Modified yield and potential surfaces in meridional stress space; dark zone shows the corner region issue tackled with tension cap; constant aspect ratio $R = a/b$ denotes the eccentricity of the cap surface; the hardening compression cap initiates at the point with zero horizontal tangency, $\partial g/\partial I_1 = 0$. $\partial g/\partial \sigma$ represents the direction of the plastic increment vector under nonassociated plastic flow rule.

As shown in Fig. 3, the plastic strain increment vector (which is perpendicular to the plastic potential surface for nonassociated plastic flow) is horizontal at two extremities T and X. This characteristic is in accordance with reality in that no incremental deviatoric plastic strain develops for hydrostatic compression and tension load paths.

2.3.2. EVOLUTION LAWS FOR ISOTROPIC/KINEMATIC HARDENING PARAMETERS

The use of an inadequate number of internal variables, which describe multiple aspects of failure modes, contributes to an inaccurate mechanical response prediction, especially when a model is implemented in a large-scale finite element analysis. The inelastic deformation of geomaterials is commonly categorized into the brittle or ductile fields and the failure mode may undergo a transition from one field to another [13,45]. Under low confinement, inelastic deformation primarily involves shear deformation along with volumetric dilation induced by the microcracking and frictional sliding of the grain fragments. At the higher level of deviatoric stress, the brittle faulting mode culminates in strain localization which appears in the form of shear or combined shear/dilation bands. As the confining pressure increases, deformation mechanisms including grain crushing and pore collapse will become predominant, leading ultimately to compactant cataclastic flow. This ductile flow commonly operates in a delocalized manner and is accompanied by shear-enhanced compaction and strain hardening phenomena.

In this study, the plasticity model is furnished with two internal variables, $\boldsymbol{\alpha}$ and κ. In the shear regime, the deviatoric back stress tensor $\boldsymbol{\alpha}$ is adopted to produce directional effects on the kinetics of the plastic flow (the so-called Bauschinger effect). Particularly, while stress-induced microcracks begin to propagate through the material, initial yield surface is permitted to translate with respect to the hydrostatic axis toward the failure envelope. The contact of the translated yield surface with this limit may indicate the inception of the softening localization due to growth and coalescence of microcracks. Evolution of the back stress is related to the deviatoric plastic strain and consequently takes the following form:

$$\boldsymbol{h^{\alpha}(\alpha)} \;=\; c^{\alpha} G^{\alpha}\, dev\left(\frac{\dot{\boldsymbol{\varepsilon}}^{\boldsymbol{p}}}{\left\|\dot{\boldsymbol{\varepsilon}}^{\boldsymbol{p}}\right\|}\right) = \; c^{\alpha} G^{\alpha}\left(\frac{\partial g}{\partial \boldsymbol{\sigma}} - \frac{\partial g}{\partial I_1}\mathbf{1}\right) \tag{18}$$

Above, c^{α} is a constant that controls the rate of hardening. The scalar function G^{α} restricts the growth of the back stress as it approaches the failure surface. This modulator is computed by

$$G^{\alpha} = 1 - \left(\frac{\boldsymbol{\alpha} \,:\, \boldsymbol{\alpha}}{2N^2}\right)^{\frac{1}{2}} \tag{19}$$

For the compactant cataclastic flow regime, a scalar hardening parameter κ is defined, associated with the cap surface, to endow the yield surface with isotropic expansion. As extensively discussed in [46], describing the grain crushing through the progressive loss of material integrity is disputable. Hence, this deformation mechanism should be regarded as the evolution to a less porous and stronger state [20].

The evolution of κ related to isotropic hardening, is given as

$$h^{\kappa}(\kappa) = \frac{tr\left(\frac{\dot{\boldsymbol{\varepsilon}}^{\boldsymbol{p}}}{\left\|\dot{\boldsymbol{\varepsilon}}^{\boldsymbol{p}}\right\|}\right)}{\frac{d\varepsilon_v^p}{d\kappa}} = \frac{3\,\frac{\partial g}{\partial I_1}}{\left(\frac{\partial \varepsilon_v^p}{\partial X}\frac{\partial X}{\partial \kappa}\right)} \tag{20}$$

Here, the following form of volumetric plastic strain is used.

$$\varepsilon_v^p = W\{exp[D_1\ (X(\kappa) - X_0)\ -\ D_2\ (X(\kappa) - X_0)^2] - 1\} \quad (21)$$

In the above, W, D_1 and D_2 are material parameters, $X_0 = X(\kappa_0)$ is the end point of initial cap, and κ_0 is the initial value for cap parameter. To be more descriptive, combined isotropic/kinematic hardening of the cap model is visualized by the schematic diagram in Fig. 4. It should be mentioned that although the softening-induced localization behavior is also of importance in many geological and geophysical problems [43,47–50], it is beyond the scope of the present paper and will be discussed in the future work.

2.3.3. RATE-DEPENDENT MODEL

The viscoplasticity is taken into account using the type of overstress model originally proposed by Duvaut and Lions [51]. A viscoplastic strain rate, $\dot{\boldsymbol{\varepsilon}}^{vp}$, is adopted rather than $\dot{\boldsymbol{\varepsilon}}^{p}$ to express the rate-dependent constitutive equations as below

$$\dot{\boldsymbol{\varepsilon}}^{vp} = \frac{1}{\eta}\ \boldsymbol{C}^{e^{-1}} : (\boldsymbol{\sigma} - \tilde{\boldsymbol{\sigma}}) \quad (22a)$$

$$\begin{Bmatrix} \dot{\boldsymbol{\alpha}} \\ \dot{\kappa} \end{Bmatrix} = \frac{-1}{\eta} \begin{Bmatrix} \boldsymbol{\alpha} - \tilde{\boldsymbol{\alpha}} \\ \kappa - \tilde{\kappa} \end{Bmatrix} \quad (22b)$$

here, $\tilde{\boldsymbol{\sigma}}, \tilde{\boldsymbol{\alpha}}$ and $\tilde{\kappa}$ are solutions for the rate-independent case. The relaxation time $\eta \in (0, \infty)$ is devised to the formula such that for the lower bound ($\eta \to 0^+$), the inviscid solution is obtained and we attain the elastic solution when $\eta \to \infty$. This model is numerically appealing due to its simplicity and ability to exploit the existing framework of classical rate-independent plasticity.

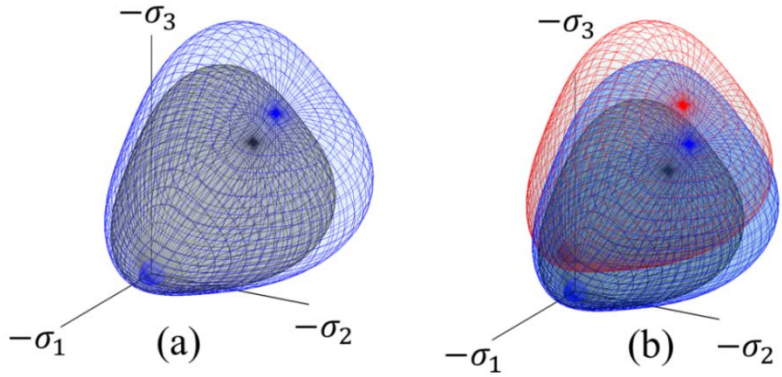

Fig. 4. Three-dimensional view of initial yield surface (the interior gray solid) evolution in principal stress space for: (a) isotropic hardening and (b) mixed isotropic-kinematic hardening.

20 NUMERICAL IMPLEMENTATION

In this section, the numerical implementation of the proposed model is presented. Since analytical solutions are almost never available for complex boundary value problems, this step is essential for application of the model to engineering problems. In addition to the addition of the tension cap and form of the yield function mentioned previously, we have made some modification to the numerical algorithm as described below. In particular, we have modified the residual to have uniform units, improving the robustness of the Newton-Raphson procedure, in Section 3.2.1. Additionally, we have developed a method to determine whether the stress is on the shear surface or cap surface for the trial state, as discussed in Section 3.2.3. This modification improves efficiency as the number of active

internal state variables changes depending on which part of the yield surface the stress state lies. Previously, one had to guess which part of the yield surface the stress state was on, and run a second set of iterations if the first guess was incorrect.

20.1 IMPLICIT INTEGRATION ALGORITHM

Let $[0, \mathrm{T}] \subset \mathrm{R}$ be the time interval of interest. At time $t_n \in [0, \mathrm{T}]$, the values of plastic strain, stress and internal state variables are known from the previous analysis. Considering a strain-driven problem, we attempt to update these variables to t_{n+1} via the evolution equations in (2), (6) and (7) for a given strain increment, $\boldsymbol{\Delta\varepsilon}_{n+1}$. The well-established stress integration algorithm recognized as a predictor-corrector method (often called return mapping) is adopted. Consequently, in the first step, the elastic trial stress $\boldsymbol{\sigma}_{n+1}^{tr} = \boldsymbol{\sigma}_n + \boldsymbol{C^e}\!:\boldsymbol{\Delta\varepsilon}_{n+1}$ is estimated by freezing plastic flow during the time step $[t_n, t_{n+1}]$, and in the second step, the plastic flow rule, Eq. (7), is applied together with optimality conditions to find a point projection of the trial stress state, (i.e. $\{\boldsymbol{\sigma}_{n+1}, \boldsymbol{\alpha}_{n+1}, \kappa_{n+1}, \gamma_{n+1}\}$), onto the updated curve of the yield surface, f_{n+1}. In addition, fully implicit or backward Euler difference scheme is employed to derive evolution equations and conditions in the discrete form. This approximate numerical technique provides first-order accuracy as well as unconditional stability even for larger strain increments by comparison, traditional explicit and semi-implicit integration schemes exhibit only conditional stability. The Newton-Raphson (N-R) iterative method is used and hence the system has to be solved as many times as required to converge to the final solution.

$$\boldsymbol{X}_{n+1}^{k+1} = \boldsymbol{X}_{n+1}^{k} - \left[\left(\frac{D\boldsymbol{R}}{D\boldsymbol{X}}\right)_{n+1}^{k}\right]^{-1} \boldsymbol{R}_{n+1}^{k} \tag{23}$$

in which $\boldsymbol{X}$ and $\boldsymbol{R}$ denote the vectors of unknown variables and residual, respectively; k + 1 refers to the current iteration. The inverse of matrix $D\boldsymbol{R}/D\boldsymbol{X}$ is not explicitly computed, and the equations are solved using Gaussian elimination.

$$\boldsymbol{X} = \{\sigma_{11}\ \sigma_{22}\ \sigma_{33}\ \sigma_{23}\ \sigma_{31}\ \sigma_{12}\ \alpha_{11}\ \alpha_{22}\ \ \alpha_{12}\ \alpha_{31}\ \alpha_{12}\ \kappa\ \Delta\gamma\}^t \tag{24a}$$

$$\text{and, } \boldsymbol{R} = \begin{Bmatrix} -\Delta\gamma c_{11kl}^{e}(\partial g/\partial\sigma_{kl}) - \sigma_{11} + \sigma_{11}^{tr} \\ -\Delta\gamma c_{22kl}^{e}(\partial g/\partial\sigma_{kl}) - \sigma_{22} + \sigma_{22}^{tr} \\ -\Delta\gamma c_{33kl}^{e}(\partial g/\partial\sigma_{kl}) - \sigma_{33} + \sigma_{33}^{tr} \\ -\Delta\gamma c_{23kl}^{e}(\partial g/\partial\sigma_{kl}) - \sigma_{23} + \sigma_{23}^{tr} \\ -\Delta\gamma c_{31kl}^{e}(\partial g/\partial\sigma_{kl}) - \sigma_{31} + \sigma_{31}^{tr} \\ -\Delta\gamma c_{12kl}^{e}(\partial g/\partial\sigma_{kl}) - \sigma_{12} + \sigma_{12}^{tr} \\ \Delta\gamma(h^{\alpha})_{11} - \alpha_{11} + \alpha_{11}^{tr} \\ \Delta\gamma(h^{\alpha})_{22} - \alpha_{22} + \alpha_{22}^{tr} \\ \Delta\gamma(h^{\alpha})_{23} - \alpha_{23} + \alpha_{23}^{tr} \\ \Delta\gamma(h^{\alpha})_{31} - \alpha_{31} + \alpha_{31}^{tr} \\ \Delta\gamma(h^{\alpha})_{12} - \alpha_{12} + \alpha_{12}^{tr} \\ \Delta\gamma h^{\kappa} - \Delta\kappa \\ f \end{Bmatrix}_{13\times 1} = 0, \tag{24b}$$

where subscript $n + 1$ is left off to simplify notation. Here $\alpha_{33} = -(\alpha_{11} + \alpha_{22})$ can be eliminated since the backstress is deviatoric. Fig. 5 demonstrates the return mapping algorithm used for nonassociated plasticity.

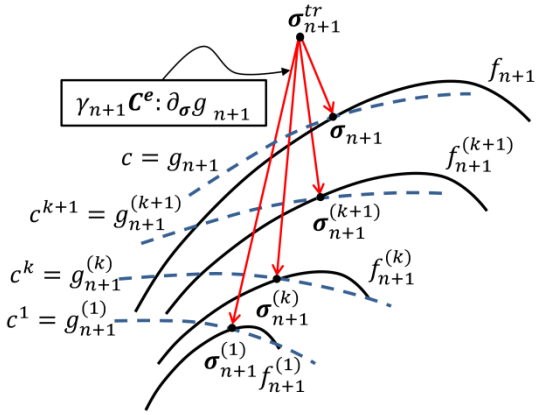

Fig. 5. Schematic interpretation of the implicit return mapping procedure under non-associated plastic flow in 2D stress space; (k+1) indicates the current iteration.

It is well known that to obtain a quadratic rate of convergence for global-level iterations, a tangent matrix must be formulated in a manner consistent with the update algorithm, Eq. (24b) [52]. For a converged solution a variation in strain does not cause a variation of the residuals. In other words:

$$\left(\frac{D\boldsymbol{R}}{D\boldsymbol{\varepsilon}}\right)_{n+1} = \left(\frac{\partial \boldsymbol{R}}{\partial \boldsymbol{\varepsilon}}\right)_{n+1} + \left(\frac{\partial \boldsymbol{R}}{\partial \boldsymbol{X}}\right)_{n+1} \cdot \left(\frac{\partial \boldsymbol{X}}{\partial \boldsymbol{\varepsilon}}\right)_{n+1} = 0 \tag{25a}$$

The term $(\partial \boldsymbol{R}/\partial \boldsymbol{\varepsilon})_{n+1}$ can be obtained and moved to the RHS as below

$$\left(\frac{\partial \boldsymbol{R}}{\partial \boldsymbol{X}}\right)_{13\times13}\left(\frac{\partial \boldsymbol{X}}{\partial \boldsymbol{\varepsilon}}\right)_{13\times6} = -\left(\frac{\partial \boldsymbol{R}}{\partial \boldsymbol{\varepsilon}}\right)_{13\times6} = \begin{bmatrix}-[\boldsymbol{C^e}]_{6\times6}\\ [\boldsymbol{0}]_{7\times6}\end{bmatrix}_{13\times6} \tag{25b}$$

therefore

$$\left(\frac{\partial \boldsymbol{X}}{\partial \boldsymbol{\varepsilon}}\right)_{13\times6} = \left(\frac{\partial \boldsymbol{R}}{\partial \boldsymbol{X}}\right)^{-1}_{13\times13}\begin{bmatrix}-[\boldsymbol{C^e}]_{6\times6}\\ [\boldsymbol{0}]_{7\times6}\end{bmatrix}_{13\times6} \tag{25c}$$

which can be rewritten as

$$\left(\frac{\partial \boldsymbol{X}}{\partial \boldsymbol{\varepsilon}}\right)_{13\times6} = \underbrace{\begin{bmatrix}(\boldsymbol{C^e})^{-1} + \Delta\gamma\dfrac{\partial^2 g}{\partial\boldsymbol{\sigma}\partial\boldsymbol{\sigma}} & \Delta\gamma\dfrac{\partial^2 g}{\partial\boldsymbol{\sigma}\partial\boldsymbol{q}} & \dfrac{\partial g}{\partial\boldsymbol{\sigma}}\\ -\Delta\gamma\left(\dfrac{\partial \boldsymbol{h}^q}{\partial\boldsymbol{\sigma}}\right) & \boldsymbol{1} - \Delta\gamma\left(\dfrac{\partial \boldsymbol{h}^q}{\partial\boldsymbol{\sigma}}\right) & -\boldsymbol{h}^q\\ \left(\dfrac{\partial f}{\partial\boldsymbol{\sigma}}\right)^t & \left(\dfrac{\partial f}{\partial\boldsymbol{q}}\right)^t & 0\end{bmatrix}^{-1}}_{\boldsymbol{A}_{13\times13}}\begin{bmatrix}[\boldsymbol{I}]_{6\times6}\\ [\boldsymbol{0}]_{7\times6}\end{bmatrix}_{13\times6} \tag{25d}$$

And hence, the consistent tangent operator $\boldsymbol{C}_{n+1} = (\partial\boldsymbol{\sigma}/\partial\boldsymbol{\varepsilon})_{n+1}$, the upper left 6-by-6 submatrix of $(\partial\boldsymbol{X}/\partial\boldsymbol{\varepsilon})_{n+1}$, can be derived from the upper left 6-by-6 submatrix of $\boldsymbol{A}$. It should be noted that for a nonassociative model, the consistent tangent modulus and resulting stiffness matrix lose their major symmetry. This asymmetric property may lead to more intensive computations. Thus, appropriate algorithms must be applied so that the inverse can be found much more efficiently

20.2 EFFICIENCY AND ROBUSTNESS IMPROVEMENTS FOR NUMERICAL COMPUTATIONS

In elastoplastic analyses, the use of an efficient algorithm plays a key role in the numerical implementation to work in a general boundary-value problem. In order to improve computational efficiency particular mathematical treatments may be noted.

3.2.1. UNIFORM DIMENSIONALITY

The residual vector $\boldsymbol{R}$ with the lack of uniform dimensionality may considerably reduce efficiency of the iterative equation solver, Eq. (23), as increase the condition number (the ratio between the largest and smallest eigenvalues) of the local tangent operator $D\boldsymbol{R}/D\boldsymbol{X}$. However, we have revised Eq. (12) such that it now has units of stress rather than stress squared. Aligning the units of this equation with the other equations in the residual vector improves the conditioning of the local tangent matrix so that the inverse matrix $(D\boldsymbol{R}/D\boldsymbol{X})^{-1}$ can be found much more effectively. In addition, as described in Box 1, because of the nature of the residual vector, convergence of each component should be fulfilled. As pointed out by Foster et al. [34], in some examples one larger component may hamper the quadratic convergence of other components and consequently increases the number of iterations needed to obtain the final solutions. This drawback is also solved by the use of new format of the yield function.

3.2.2. RETURN MAPPING ALGORITHM IN PRINCIPAL STRESS AXES

The standard return mapping algorithm in principal stress axes was first adopted for isotropic plasticity models [53,54]; accordingly, the iterative equation solver needs to evaluate only the principal values of the state variables. Thereafter, Foster et al. [34] extended the application to the models which include kinematic hardening by spectrally decomposing the relative stress $\boldsymbol{\xi}$**.** To facilitate computations, an alternative variable, called the plastic corrector $\boldsymbol{\sigma}_{n+1}^{corr} \coloneqq \boldsymbol{\sigma}_{n+1} - \boldsymbol{\sigma}_{n+1}^{tr}$, was defined for the stress increment. Therefore, the reduced form of the unknown variables and residual vector can be obtained as below

$$\boldsymbol{X} = \{\sigma_I^{corr} \quad \sigma_{II}^{corr} \quad \sigma_{III}^{corr} \quad \Delta\alpha_I \quad \Delta\alpha_{II} \quad \Delta\kappa \quad \Delta\gamma\}^t \tag{26a}$$

$$\text{and, } \boldsymbol{R} = \begin{Bmatrix} \Delta\gamma a_{1A}^e(\partial g/\partial\sigma_A) + \sigma_I^{corr} \\ \Delta\gamma a_{2A}^e(\partial g/\partial\sigma_A) + \sigma_{II}^{corr} \\ \Delta\gamma a_{3A}^e(\partial g/\partial\sigma_A) + \sigma_{III}^{corr} \\ \Delta\gamma(h^\alpha)_I - \Delta\alpha_I \\ \Delta\gamma(h^\alpha)_{II} - \Delta\alpha_{II} \\ \Delta\gamma h^\kappa - \Delta\kappa \\ f \end{Bmatrix}_{7\times1} = 0, \tag{26b}$$

where subscript $n + 1$ is left off. $A=1, 2, 3$ indicates the principal direction. $\Delta\alpha_{III} = -\Delta\alpha_I - \Delta\alpha_{II}$ is eliminated since the back stress is deviatoric.

$$\boldsymbol{a}^e = \begin{bmatrix} \lambda+2\mu & \lambda & \lambda \\ \lambda & \lambda+2\mu & \lambda \\ \lambda & \lambda & \lambda+2\mu \end{bmatrix} \tag{27a}$$

$$h_B^\alpha(\boldsymbol{\alpha}) = c^\alpha G^\alpha \left(\frac{\partial g}{\partial \sigma_B} - \frac{\partial g}{\partial I_1}\right) \tag{27b}$$

The tensor $\boldsymbol{a}^e$ is the elasticity tensor projected to principal relative stress space.
In the case of kinematic hardening, one can see that

$$\frac{\partial g}{\partial \sigma_B} = \frac{\partial g}{\partial \xi_B}\frac{\partial \xi_B}{\partial \sigma_B} = \frac{\partial g}{\partial \xi_B} \tag{28}$$

It has been shown that $\boldsymbol{\xi}_{n+1}^{tr}$, $\boldsymbol{\xi}_{n+1}, \boldsymbol{\sigma}_{n+1}^{corr}$ and $\Delta\boldsymbol{\alpha}_{n+1}$ share the same spectral directions (for more details the reader is referred to [34]). These directions may be determined from $\boldsymbol{\xi}_{n+1}^{tr}$, which is known a priori. Hence, once the principal values of $\boldsymbol{\sigma}^{corr}$ and $\Delta\boldsymbol{\alpha}$ are determined, these tensorial variables can be obtained as follows

$$\boldsymbol{n}_{\boldsymbol{\sigma}^{corr}}^{(A)} \; and \; \boldsymbol{n}_{\Delta\alpha}^{(A)} \parallel \boldsymbol{n}_{\xi^{tr}}^{(A)} \Longrightarrow \begin{cases} \boldsymbol{\sigma}^{corr} = \sum_{A=1}^{3} \sigma_A^{corr}\, \boldsymbol{n}_{\xi^{tr}}^{(A)} \otimes \boldsymbol{n}_{\xi^{tr}}^{(A)} \\ \Delta\boldsymbol{\alpha} = \sum_{A=1}^{3} \Delta\alpha_A\, \boldsymbol{n}_{\xi^{tr}}^{(A)} \otimes \boldsymbol{n}_{\xi^{tr}}^{(A)} \end{cases} \tag{29}$$

where $\boldsymbol{n}^{(A)}$ denotes the corresponding eigenvectors.
Afterwards, the updated stress and back stress tensors can be easily computed by.

$$\boldsymbol{\sigma}_{n+1} = \boldsymbol{\sigma}_{n+1}^{corr} + \boldsymbol{\sigma}_{n+1}^{tr} \tag{30a}$$
$$\boldsymbol{\alpha}_{n+1} = \boldsymbol{\alpha}_n + \Delta\boldsymbol{\alpha}_{n+1} \tag{30b}$$

3.2.3. A PRIORI SHEAR/CAP SURFACE DETERMINATION

The plastic model hypothesizes that the compression cap characterizes hardening behavior, not softening, graphically illustrated in Fig. 6. This assumption is in agreement with the physical behavior of geological materials in compactant cataclastic flow regime [46,55]. Hence, κ is not allowed to increase, and remains constant meanwhile the stress path is proceeding along the shear surface in which the kinematic hardening solely operates (with no isotropic hardening participation).

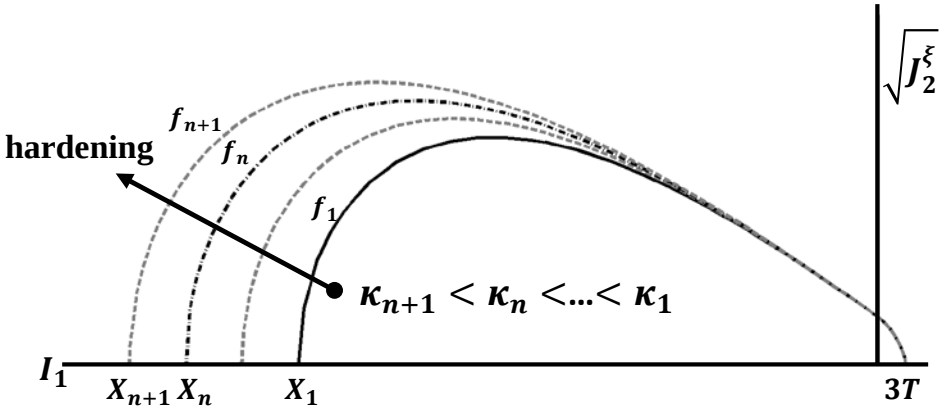

Fig. 6. Hardening behavior of compression cap in meridional stress space

Accordingly, we utilize the restriction $\dot{\kappa} \leq 0$ to modify the number of unknown variables for the residual vector by differentiating between the compactive compression cap and the shear surface. It is worth remarking here there is some ambiguity in the literature for smooth cap models as to where the cap surface begins. For this article the cap surface refers to the portion of the yield surface with $\partial g/\partial I_1 < 0$, i.e. where compaction hardening may occur. This distinction is different from some authors who begin the cap surface at κ (in non-smooth cap models, they are identical). While the yield surface is still affected by the cap function between κ and the point where $\partial g/\partial I_1 = 0$, the fact that compaction hardening cannot occur, along with the implementational concerns already discussed, justifies the distinction chosen here.

As shown in Eq. (31), $\partial g/\partial I_1$ has the same sign as $\dot{\kappa}$ since the rest of factors $\dot{\gamma}$, $\partial \varepsilon_v^p/\partial X$ and $\partial X/\partial \kappa$ are always positive. As a result, the hardening cap is active when ($\partial g/\partial I_1$) < 0 and otherwise, κ keeps its value from the previous step.

$$\dot{\kappa} = \begin{cases} \dfrac{3\dot{\gamma}\left(\dfrac{\partial g}{\partial I_1}\right)}{\left(\dfrac{\partial \varepsilon_v^p}{\partial X}\dfrac{\partial X}{\partial \kappa}\right)}, & \partial g/\partial I_1 < 0 \\ 0 \quad , & \partial g/\partial I_1 \geq 0 \end{cases} \tag{31}$$

It may be shown $\partial g/\partial I_1$ shares the same sign as $\partial g/\partial I_1^{tr}$. This fact is proven in the appendix. Hence, it can be determined, from the trial stress state, whether or not κ needs to be evaluated as below:

$$\boldsymbol{R} = \begin{cases} \begin{Bmatrix} \Delta\gamma a_{1A}^e(\partial g/\partial \xi_A) + \sigma_I^{corr} \\ \Delta\gamma a_{2A}^e(\partial g/\partial \xi_A) + \sigma_{II}^{corr} \\ \Delta\gamma a_{3A}^e(\partial g/\partial \xi_A) + \sigma_{III}^{corr} \\ \Delta\gamma(h^\alpha)_I - \Delta\alpha_I \\ \Delta\gamma(h^\alpha)_{II} - \Delta\alpha_{II} \\ \Delta\gamma h^\kappa - \Delta\kappa \\ f \end{Bmatrix}_{7\times 1}, & \dfrac{\partial g}{\partial I_1^{tr}} < 0 \\ \begin{Bmatrix} \Delta\gamma a_{1A}^e(\partial g/\partial \xi_A) + \sigma_I^{corr} \\ \Delta\gamma a_{2A}^e(\partial g/\partial \xi_A) + \sigma_{II}^{corr} \\ \Delta\gamma a_{3A}^e(\partial g/\partial \xi_A) + \sigma_{III}^{corr} \\ \Delta\gamma(h^\alpha)_I - \Delta\alpha_I \\ \Delta\gamma(h^\alpha)_{II} - \Delta\alpha_{II} \\ f \end{Bmatrix}_{6\times 1}, & \dfrac{\partial g}{\partial I_1^{tr}} \geq 0 \end{cases} \tag{32}$$

This knowledge may increase efficiency of the stress computation as it eliminates an extra set of N-R iterations. Indeed, in the previous formulation, the full-variable N-R iteration is performed regardless of where the stress path proceeds on the updated yield surface. In the case that the shear surface is activated, it generates the spurious solutions including a positive $\Delta\kappa$. Thus, another N-R iteration needs to be carried out, this time, eliminating $\Delta\kappa$ and its correspondent evolution equation from the system of equations.

We outline the implicit stress-integration algorithm in Box 1.

Box 1. Summary of implicit stress-point algorithm

Given: $\boldsymbol{\sigma}_n$, κ_n, $\boldsymbol{\alpha}_n$ and $\Delta\boldsymbol{\varepsilon}_{n+1}$
Goal: $\boldsymbol{\sigma}_{n+1}$, κ_{n+1}, $\boldsymbol{\alpha}_{n+1}$
Step 1. compute trail elastic state:
$\boldsymbol{\sigma}_{n+1}^{\mathrm{tr}} = \boldsymbol{\sigma}_n + \mathbf{C^e}\colon\Delta\boldsymbol{\varepsilon}_{n+1}$, $\boldsymbol{\alpha}_{\mathbf{n+1}}^{\mathbf{tr}} = \boldsymbol{\alpha}_n$, $\kappa_{n+1}^{tr} = \kappa_n$
Step 2. Apply spectral decomposition:
$\boldsymbol{\xi}_{n+1}^{tr} = \boldsymbol{\sigma}_{n+1}^{tr} - \boldsymbol{\alpha}_n = \sum_{A=1}^{3} \xi_A^{tr}\, \boldsymbol{n}_{\xi^{tr}}^{(A)} \otimes \boldsymbol{n}_{\xi^{tr}}^{(A)}$ and set $\boldsymbol{n}_{\boldsymbol{\sigma}^{corr}}^{(A)} = \boldsymbol{n}_{\Delta\alpha}^{(A)} = \boldsymbol{n}_{\xi^{tr}}^{(A)}$
Step 3. Check yielding: is $f_{n+1}^{tr} > 0$?
If no, set $\boldsymbol{\sigma}_{n+1} = \boldsymbol{\sigma}_{n+1}^{tr}$, $\boldsymbol{\alpha}_{n+1} = \boldsymbol{\alpha}_n$, $\kappa_{n+1} = \kappa_n$ and exit.

If yes, go to step 4

Step 4. Determine whether we are on shear or cap surface:

Check $(\partial g/\partial I_1^{tr})_{n+1} \geq 0$?

If yes, set $\boldsymbol{X}_{0_{6\times1}} = \mathbf{0}, \Delta\kappa = 0$ and iterate:

$\delta\boldsymbol{X}_{6\times1}^{k+1} = [(D\boldsymbol{R}/D\boldsymbol{X})^k]_{6\times6}^{-1}\boldsymbol{R}(\boldsymbol{X}^k)_{6\times1}$

$\boldsymbol{X}_{6\times1}^{k+1} = \boldsymbol{X}_{6\times1}^{k} + \delta\boldsymbol{X}_{6\times1}^{k+1}$

until $(R_{\boldsymbol{\sigma}}/R_{\boldsymbol{\sigma},\max}) < \text{tol}_{\boldsymbol{\sigma}}$, $(R_{\boldsymbol{\alpha}}/R_{\boldsymbol{\alpha},\max}) < \text{tol}_{\boldsymbol{\alpha}}$, , and $(R_f/R_{f,\max}) < \text{tol}_f$

If no, set $\boldsymbol{X}_{0_{7\times1}} = \mathbf{0}$ and iterate:

$\delta\boldsymbol{X}_{7\times1}^{k+1} = [(D\boldsymbol{R}/D\boldsymbol{X})^k]_{7\times7}^{-1}\boldsymbol{R}(\boldsymbol{X}^k)_{7\times1}$

$\boldsymbol{X}_{7\times1}^{k+1} = \boldsymbol{X}_{7\times1}^{k} + \delta\boldsymbol{X}_{7\times1}^{k+1}$

until $(R_{\boldsymbol{\sigma}}/R_{\boldsymbol{\sigma},\max}) < \text{tol}_{\boldsymbol{\sigma}}$, $(R_{\boldsymbol{\alpha}}/R_{\boldsymbol{\alpha},\max}) < \text{tol}_{\boldsymbol{\alpha}}$, $(R_{\kappa}/R_{\kappa,\max}) < \text{tol}_{\kappa}$, and $(R_f/R_{f,\max}) < \text{tol}_f$

Step 5. Update state variables and consistency parameter for inviscid plasticity:

$\tilde{\boldsymbol{\sigma}}_{n+1} = \boldsymbol{\sigma}_{\mathrm{n+1}}^{\mathrm{tr}} + \sum_{A=1}^{3}\sigma_A^{corr}\,\boldsymbol{n}_{\xi^{tr}}^{(A)} \otimes \boldsymbol{n}_{\xi^{tr}}^{(A)}$, $\tilde{\boldsymbol{\alpha}}_{n+1} = \boldsymbol{\alpha}_{\mathbf{n+1}}^{\mathbf{tr}} + \sum_{B=1}^{3}\Delta\alpha_A\,\boldsymbol{n}_{\xi^{tr}}^{(B)} \otimes \boldsymbol{n}_{\xi^{tr}}^{(B)}$

$\tilde{\kappa}_{n+1} = \kappa_{n+1}^{tr} + \Delta\kappa$, $\gamma_{n+1} = \gamma_n + \Delta\gamma$ and exit.

Step 6. Obtain the viscoplastic solutions

$$(\bullet)_{n+1} = \frac{(\bullet)_{n+1}^{tr}}{1 + {\Delta t}/{\eta}} + \frac{{\Delta t}/{\eta}}{1 + {\Delta t}/{\eta}}(\tilde{\bullet})_{n+1}$$

21 SIMULATION RESULTS AND DISCUSSION

In order to demonstrate various features of the modified plastic model, several numerical examples are presented. Box 2 shows material parameters for a Salem Limestone [35].

Box 2. Material properties for Salem limestone. Non-associativity introduced through L, ϕ, and Q with plot of plastic potential surface g and yield surface f shown in Fig. 1a and 3.

Young's modulus E = 22,547 (MPa)
Poisson's ratio ν = 0.2524 (dimensionless)
Isotropic tensile strength T= 5 (MPa)
$I_1^T = 0$ (MPa)
A = 689.2 (MPa)
B = 3.94e-4 (1/MPa)
L = 1.0e-4 (1/MPa)
C = 675.2 (MPa)
θ, ϕ = 0.0 (rad)
R, Q = 28.0 (dimensionless)
κ_0 = -8.05 (MPa)
W = 0.08 (dimensionless)
D_1 = 1.47e-3 (1/MPa)
D_2 = 0.0 (1/MPa^2)
c^{α} = 1e5 MPa
ψ = 0.8 (dimensionless)
N = 6.0 MPa

21.1 UNIAXIAL TENSILE EXAMPLE

First, a uniaxial tensile test is performed using a single 3D solid element to investigate numerical performance of the model with and without smooth tension cap. The mesh and boundary conditions are shown in Fig. 7. As the axial stress–strain response is shown in Fig. 8, in the case without tension cap, the model passed over the maximum uniaxial tensile strength, whereas in the modified model the material yielded sooner and axial stress coincided with the prescribed limit. In addition, the stress paths are plotted in J_2^{ξ} vs. I_1 plane, Fig. 9.

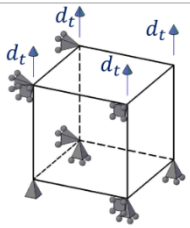

Fig. 7. Uniaxial tensile test: mesh and boundary conditions; d_t Indicates the vertical nodal displacement.

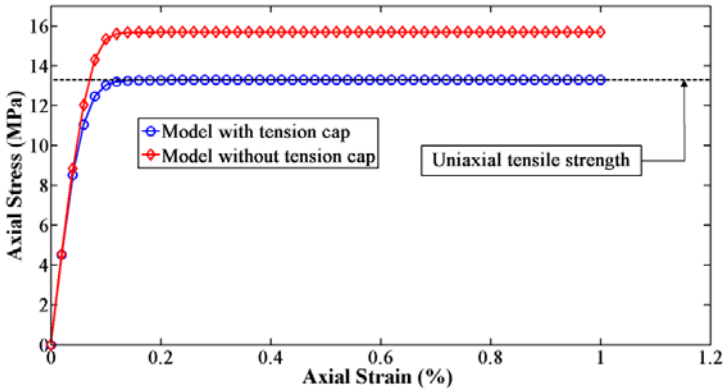

Fig. 8. Axial stress-strain response for the uniaxial tensile test.

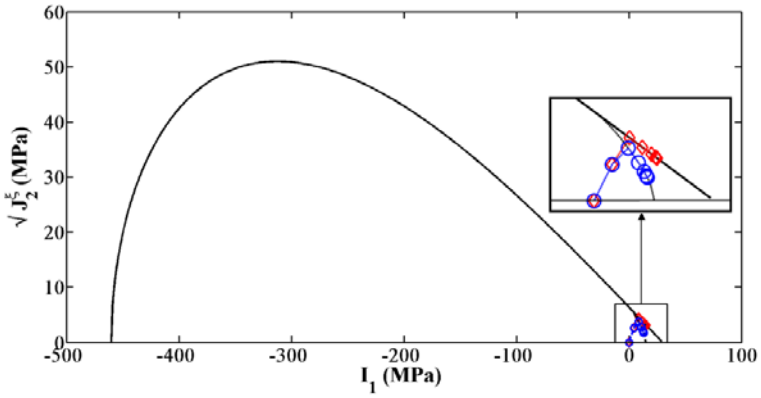

Fig. 9. Stress path in meridional stress space for the uniaxial tensile test: Model with the tension cap (circle markers); Model without the tension cap (diamond markers).

21.2 SIMPLE SHEAR EXAMPLE

In this example, a simple shear test is performed. The horizontal nodal displacement was applied on 4 nodes of the top surface so that no vertical displacement is induced, Fig. 10.

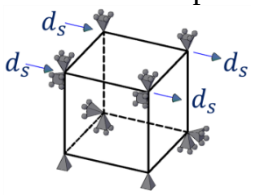

Fig. 10. Simple shear test: mesh and boundary conditions

The rate-dependent form of the model presented in Section 2.3.3 is investigated for three different η values and results are plotted in Fig. 11. The inviscid (elastoplastic) solution is attained for the lower bound ($\eta = 0$). The maximum shear stress of the material increases as the element is subjected to the shear displacements d_s with higher velocity. In addition, the volumetric response, commonly observed as a dilatant behavior at low pressure regime, is demonstrated for two associative and non-associative plastic flow rules in Fig. 12. As expected, in associative case, the dilation is overestimated compared to nonassociative model. Note that here we do not consider softening and consequently the shear strain extends to four percent. It is well known that modeling of softening requires some form of regularization, and investigation of this behavior is beyond the scope of this study.

The convergence behavior in every load step remains typical to Newton's method showing a quadratic rate of convergence for each component of the residual vector, Table 1. As discussed earlier, the uniform dimensionality generally leads to components having values in each load step with no significant difference in magnitude order from others and hence improves the overall rate of convergence for the whole residual vector.

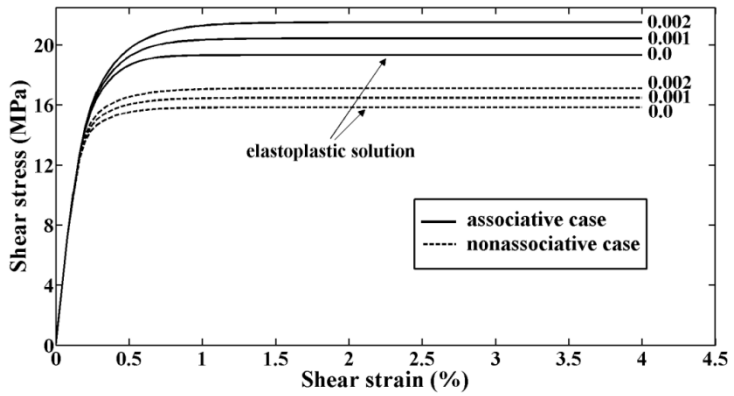

Fig. 11. Stress-strain response for selected simple shear tests of a solid element with different values of η indicated by numbers next to each curve. Examples are run for time step $\Delta t = 0.01$ and strain rate of 4% per second.

Table 1. Convergence of integration point algorithm for a simple shear test

Local residual vector $\boldsymbol{R}_{6\times1}$ (MPa)
Number of n-r iterations = 3

-2.9831e-03	2.1671e-07	-8.0491e-15
-8.3217e-03	1.3010e-06	-2.0806e-13
3.4908e-03	-1.5132e-06	2.0473e-13
1.5837e-04	-1.3682e-07	8.1297e-14
-9.6454e-05	1.2367e-07	-3.7195e-14
1.1963e-03	1.9978e-06	1.3856e-13

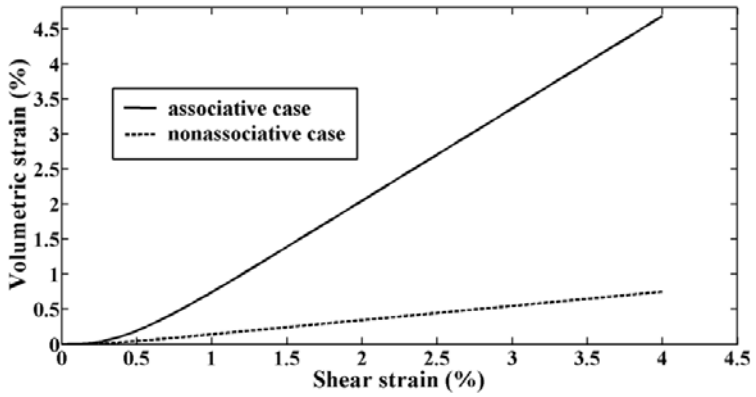

Fig. 12. Comparison of material response in associative vs. nonassociative models for selected simple shear tests of a single solid element. Results are plotted for inviscid solutions ($\eta = 0$).

21.3 TRIAXIAL COMPRESSION EXAMPLES

This test is designed to verify applicability of the model to simulate mechanical behavior under confined loading. Again, a single 3D solid element is used and subject to a force-controlled loading test with $\sigma_2 = \sigma_3 = \beta\sigma_1$, (Fig. 13). In this case, we assume the material obeys the nonassociative plastic flow rule. The stress paths for all five simulations are plotted in J_2^{ξ} vs. I_1 plane, Fig. 14. The comparative results, provided in Figs 15 (a), and (b), demonstrate how the new format of the yield function improves numerical performance of the model. For stress ratio of 0.3, the stress path successfully traverses the yield surface from shear-dilative side to the cap-compactive side. For stress ratios of 0.6, in which the combined isotropic kinematic hardening operates and the size of the yield surface needs to be updated for each next time step, the modified model completes the load schedule whereas the original version failed to converge after running few plastic steps.

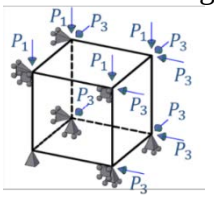

Fig. 13. Triaxial compression test: mesh and boundary conditions

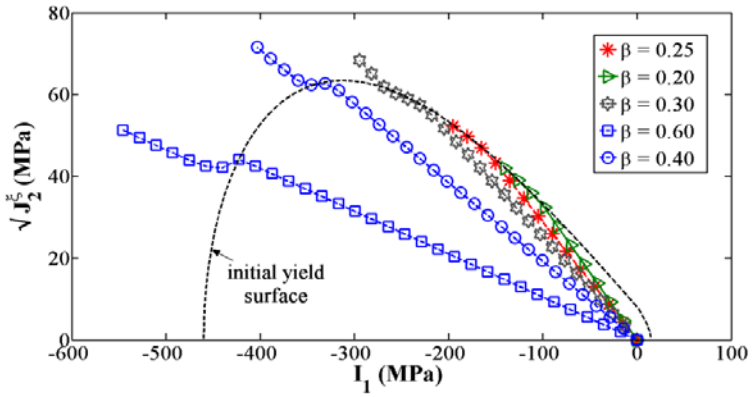

Fig. 14. Stress path in meridional stress space for selected triaxial compression examples. β denotes stress ratio σ_3/σ_1.

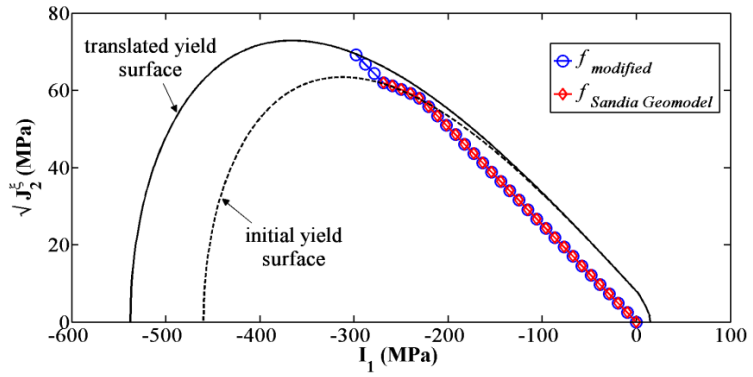

Fig. 15a. Stress path in meridional stress space for the triaxial compression test, stress ratio $\sigma_3/\sigma_1 = 0.3$.

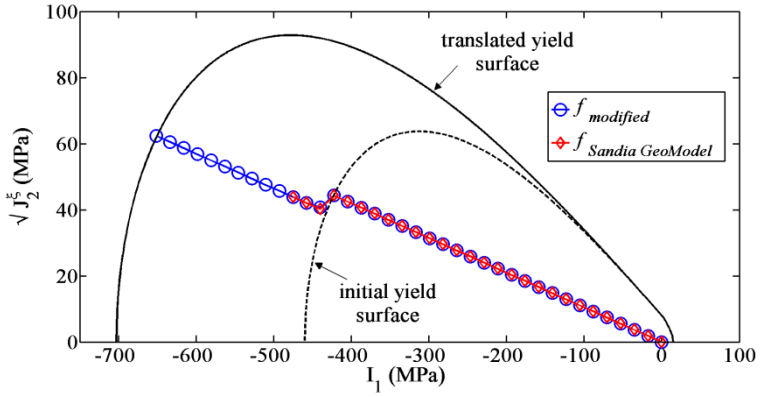

Fig. 15b. Stress path in meridional stress space for the triaxial compression test, stress ratio $\sigma_3/\sigma_1 = 0.6$.

Additional insights can be gained by comparing the strain response of the element for different stress ratio $\beta = \sigma_3/\sigma_1$. The results are computed and displayed in Figs. 16 and 17. Associated with the delocalized cataclastic flow regime, the triaxial curves (the stress ratio of 0.3 or higher) coincide with the elastic line up to a critical stress state C^* beyond which there is an accelerated decrease in volume in comparison to the hydrostatic loading. These deviations from the hydrostat would imply the volumetric strain is not only dependent on the mean stress, but also the deviatoric stresses. This phenomenon is well known as "shear-enhanced compaction" [56]. In contrast, for stress ratio of 0.25 or lower, the compaction reversed from the hydrostat beyond critical stress state marked as C', and this corresponds to the onset of dilatancy. Accordingly, these two critical stress states (C^* and C') indicate

the termination of the elastic regime and the onset of inelastic behavior. The differential stresses for two critical stress states (C^* and C') show a positive correlation with mean stress and stress ratio because the more confining pressure provides higher yield strength, and thus delays the inelastic deformation.

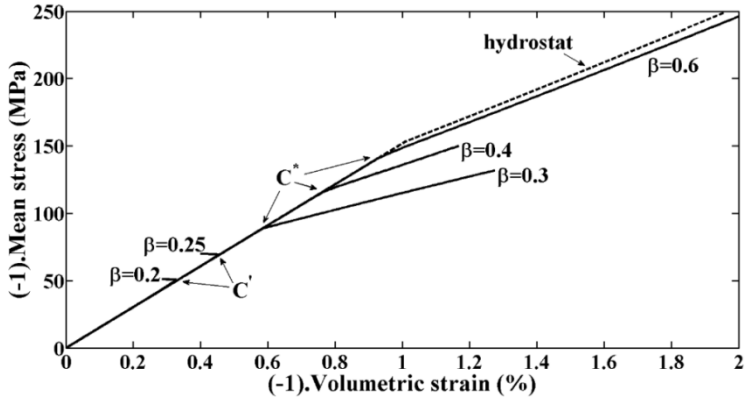

Fig. 16. Volumetric strain is plotted versus mean stress for selected triaxial compression examples. For reference the hydrostat is plotted as the dashed line. Arrows mark critical stress states (onset of dilatancy C' and onset of shear enhanced compaction C^*). β stands for stress ratio σ_3/σ_1.

At stress ratio of 0.3 or higher (in Fig. 14), the slopes of the differential stress $\sigma_1 - \sigma_3$ versus axial strain curves were positive implying the behavior which is a typical of the cataclastic flow regime. On the other hand, at stress ratio of 0.2 and 0.25 (curves marked with dash line) the differential stress became constant after reaching a peak would indicate the shear surface has reached the failure surface. As can be seen for dashed curves, the peak stress shows a positive correlation with the stress ratio and consequently confining pressure. By comparing results in Fig. 13 and Fig. 14, it is demonstrated the model can capture the shear failure as a dilatant failure mode (curves for $\beta = 0.2$ and 0.25). Overall, these numerical results are qualitatively similar to experimental data compiled in several laboratory studies for porous rocks [45,57–61]. Similar to the simple shear example, quadratic rate of convergence is obtained for local residual vectors, shown in Table 2. Moreover, as shown in Table 3 and Fig. 18, we verify the global residual vectors converge quadratically.

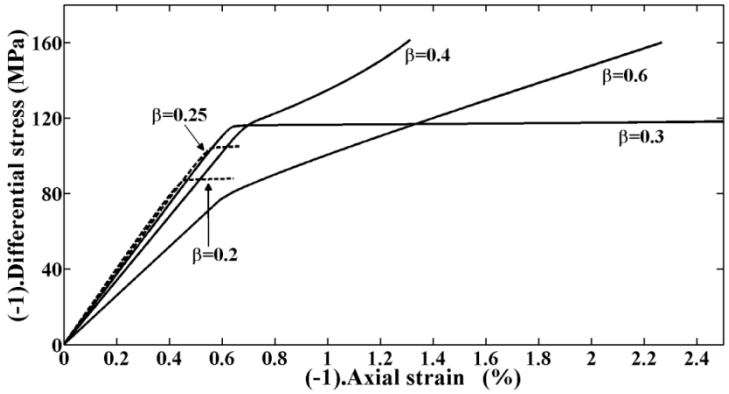

Fig. 17. Differential stress is plotted versus axial strain for selected triaxial compression examples. β stands for stress ratio σ_3/σ_1.

Table 2. Convergence of integration point algorithm for a triaxial compression test ($\boldsymbol{\beta = 0.4}$)

Local residual vector $\boldsymbol{R}_{7\times1}$ (MPa) Number of n-r iterations = 4			
6.0619e-02	4.1633e-04	2.2605e-06	2.8729e-11
6.0619e-02	4.1633e-04	2.2605e-06	2.8729e-11
6.0619e-02	4.1633e-04	2.2605e-06	2.8729e-11
6.3381e-01	-5.5378e-02	-1.9931e-04	-2.5253e-09
-3.1690e-01	2.7694e-02	9.9654e-05	1.2626e-09
3.8062e-02	2.6154e-04	1.4224e-06	1.8078e-11
5.1489e-02	1.3616e-04	1.8308e-06	2.4492e-11

Table 3. Convergence of global algorithm for a set of triaxial compression tests

Norm of the global residual vector (m)					
Iteration Number	$\beta = 0.2$	$\beta = 0.25$	$\beta = 0.3$	$\beta = 0.4$	$\beta = 0.6$
1	1.0392	1.0607	1.0863	1.1489	1.3115
2	2.6151e-02	1.1248e-02	3.8974e-02	2.4356e-02	7.3177e-02
3	3.5327e-05	5.7206e-06	6.6795e-05	2.0957e-05	9.0703e-05
4	6.5536e-11	1.4875e-12	2.0057e-10	1.5458e-11	1.0894e-09

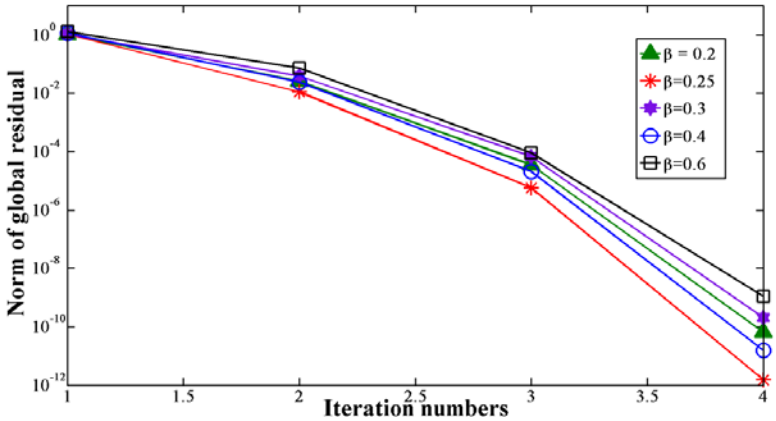

Fig. 18. Residual norm per iteration for the first plastic step in a set of triaxial compression tests.

21.4 TRIAXIAL EXTENSION VS. COMPRESSION

Here, a two-step loading test is adopted to verify the model exhibits the difference in triaxial extension strength versus triaxial compression strength for ψ = 0.8. The mesh and boundary conditions are the same as designated in Fig. 13. Therefore, in the first load step, the element is subject to hydrostatic pressure and subsequently, for triaxial extension case, the confining pressure, $P_{3,}$ increases while the axial pressure, $P_{1,}$ begins to reduce such that the mean stress keeps the value prescribed at the end of the first load step, i.e. $\Delta P_3 = -\Delta P_1/2$. Similarly, we examine the triaxial compression test by increasing the axial pressure rather than confining pressure in the second load step. Figs. 19 and 20 provide insightful views in principal stress space about the trajectory of stress evolution during two steps of loading for TXE and TXC tests, respectively. In addition, the 3D representation of initial and

translated yield surfaces are depicted. As the axial stress–strain response is shown in Figs. 21 and 22, the material yields sooner and undergoes more plastic deformation in the triaxial extension case.

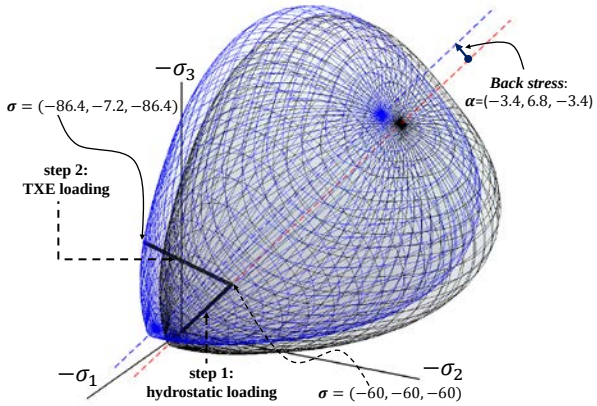

Fig. 19. Stress path for TXE in principal stress space: showing movement along the hydrostatic axis in the first load step, intersection with the initial yield surface and culminating at the final translated yield surface in the second load step.

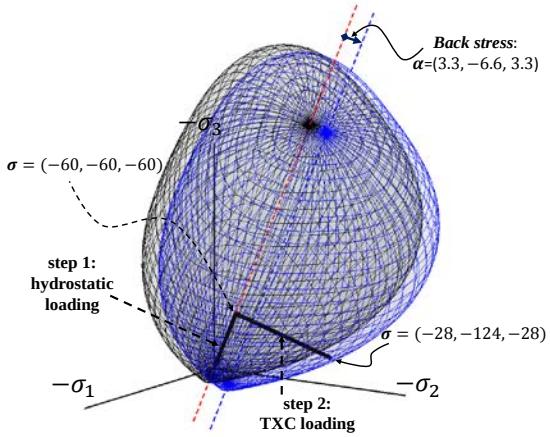

Fig. 20. Stress path for TXC in principal stress space: showing movement along the hydrostatic axis in the first load step, intersection with the initial yield surface and culminating at the final translated yield surface in the second load step.

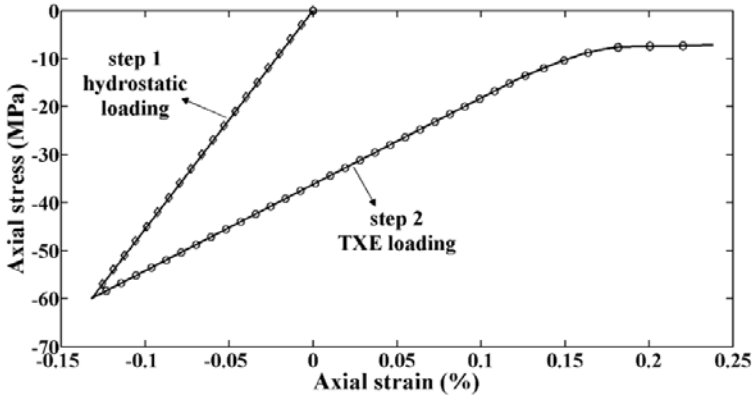

Fig. 21. Axial stress-strain response for the TXE test at the deviatoric plane with pressure $P = 60\ (MPa)$.

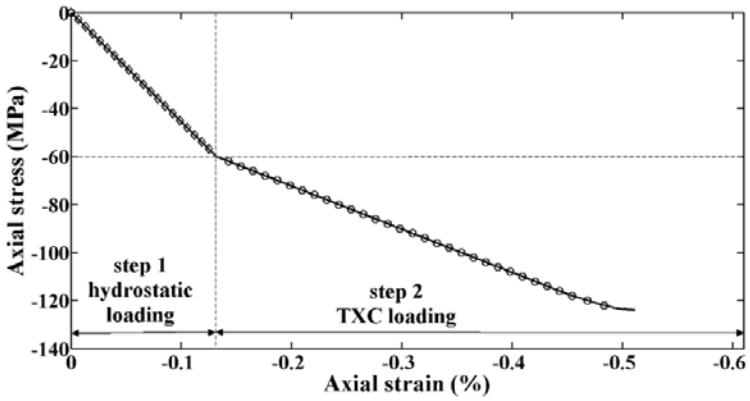

Fig. 22. Axial stress-strain response for the TXC test at the deviatoric plane with pressure $P = 60\ (MPa)$.

21.5 COMPRESSION/SHEAR EXAMPLE

This two-step loading test is designed to investigate numerical implementation of the modified model during changing spectral directions. Mesh and boundary conditions are demonstrated in Fig. 23. In the first step of loading (AC), shear displacement is set to zero, i.e. $d_s = 0$ while in the second step (CD) the compression displacement d_c and confining force P_3 are fixed to the values prescribed at the end of the first load step (C), with $P_3 = 40$ and $d_c = 0.01$. Again, we assume the material obeys the nonassociative plastic flow rule.

The stress path for the modified model and the Sandia Geomodel is plotted in the meridional stress space, Fig. 24. As can be seen, different stress paths are obtained due to the fact that the plastic flow directions of the two models are slightly different. Although the principal directions of the relative stress tensor ξ are rotating, the stress paths remain on the yield surface because the stress invariants (i.e. I_1 , J_2^{ξ}, J_3^{ξ}), used to formulate the yield functions, are independent of these changes. Moreover, the stress–strain response is plotted in Fig. 25. For both models, in the first load step, the axial response begins as elastic (AB) and then becomes plastic (BC), while the shear stress and strain remain zero along the direction marked by d_s. On the other hand, in the second load step (CD), the shear response goes to the plastic and concurrently, the compression response appears as a vertical line due to the fact that the related compressive stress drops while no deformation is induced along the d_c direction. The key difference realized between the results of two models is that during the plastic deformation (BC and CD), the modified model demonstrates more strain hardening behavior. As seen in Fig. 25, for the modified model, the slopes of the stress–strain responses show the greater values compared to Sandia Geomodel.

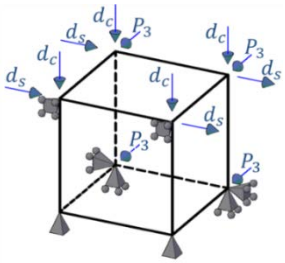

Fig. 23. Two-step loading test: mesh and boundary conditions

Tables 3 and 4 demonstrate how local iterations for residual vectors quadratically converge for the first and second steps of loading in the compression/shear example test. The resulting norm of the global residual vector is also plotted in Fig. 26 and shown in Table 6. As expected, quadratic convergence is observed.

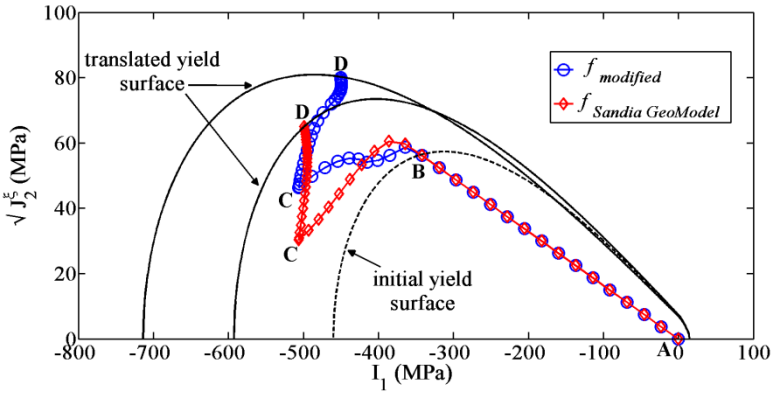

Fig. 24. Stress path in meridional stress space for the designed compression/shear test. The letters indicate points on the stress path distinguishing different phases of evolution.

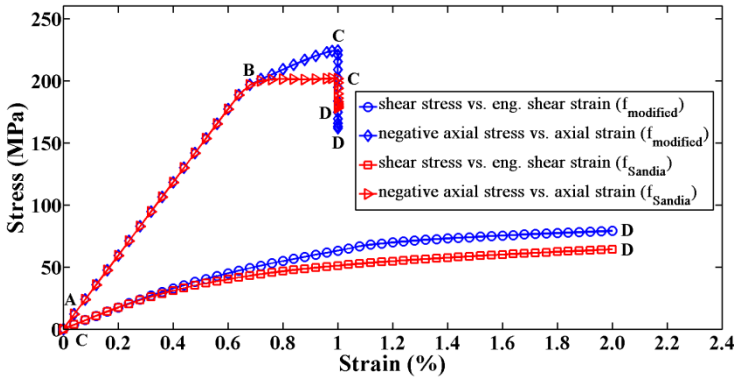

Fig. 25. Stress–strain response for a compression/shear test. The letters indicate points on the stress path distinguishing different phases of evolution.

Table 4. Convergence of integration point algorithm for the first plastic load step of compression/shear test

Local residual vector $\boldsymbol{R}_{7\times1}$ (MPa) Number of n-r iterations = 4			
1.7489e-01	2.0791e-03	4.5107e-06	2.1133e-11
1.7035e-01	2.1011e-03	4.7884e-06	2.2981e-11
1.8503e-01	2.0305e-03	3.8841e-06	1.6923e-11
3.8600e-01	-4.1568e-02	-9.6827e-05	-4.9292e-10
-3.5068e-01	3.7296e-02	8.8842e-05	4.5686e-10
1.1285e-01	1.3204e-03	2.8043e-06	1.2984e-11
1.6242e-01	4.4698e-04	5.4560e-06	2.5388e-11

Table 5. Convergence of integration point algorithm for the first shear load step of compression/shear test

Local residual vector $\boldsymbol{R}_{7\times1}$ (MPa) Number of n-r iterations = 3		
3.4037e-03	-2.0293e-07	2.3648e-14
3.4117e-03	-1.9999e-07	2.3415e-14
3.4281e-03	-1.9395e-07	2.3231e-14
4.7623e-04	-7.4150e-07	-2.5990e-13
-9.0924e-04	1.4126e-06	4.9546e-13
2.2219e-03	-1.2965e-07	1.5501e-14
2.0546e-03	1.3663e-08	-1.1369e-13

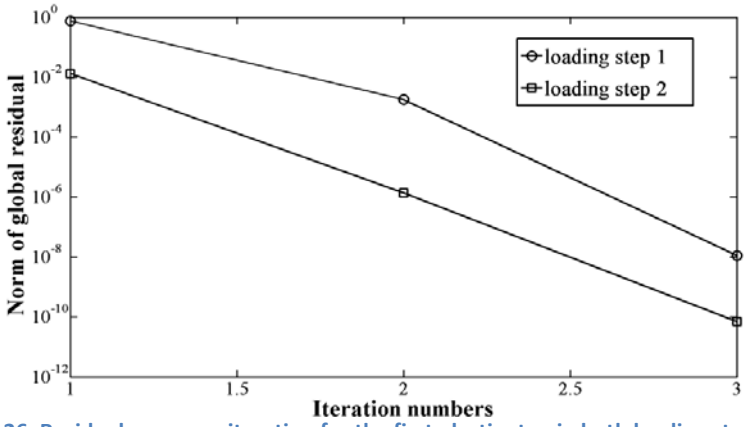

Fig. 26. Residual norm per iteration for the first plastic step in both loading steps of the compression/shear test. Quadratic convergence is observed.

Table 6. Convergence of global algorithm for the compression/shear test

Norm of the global residual vector (m)		
Iteration number	Loading step 1 (compression)	Loading step 2 (shear)
1	0.74184	0.0132
2	1.7718e-03	1.3659e-06
3	1.1222e-08	6.9587e-11

21.6 BOUNDARY VALUE PROBLEM

As a final example, a slope stability problem is presented to investigate the performance of the modified model in a full-scale non-linear finite element simulation. The dimensions and boundary conditions of the problem are depicted in Fig. 27. We assume a gravity load is first applied, then the deformation is reset to zero, and finally a downward displacement is loaded at the middle of a rigid footing resting at the crest of the slope. The downward displacement may represent the settlement due to a structure placed at the crest of the slope. Two meshes with 400 and 1600 bilinear quadrilateral

elements are used to analyze the problem. Standard 2-by-2 Gaussian integration is used. To get more realistic results, we assume the material obeys the nonassociative plastic flow rule which its parameters are given in Box 2 and set ψ=0.8 to enable SD effect attribute of the model (J_3^{ξ} dependence). Deformed shapes are scaled by factor of 10.

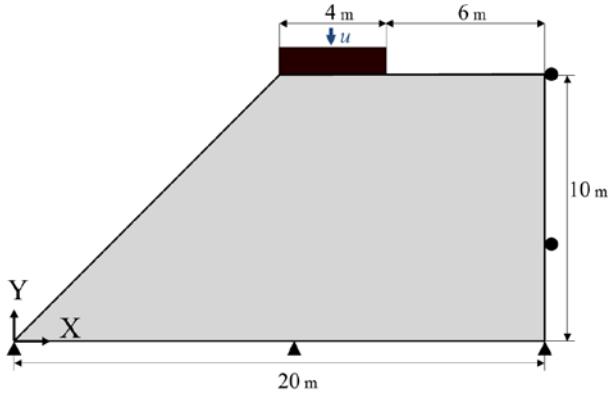

Fig. 27. Slope stability problem. Gravity load applied before footing displacement *u* is prescribed.

Figs. 28 and 29 illustrate deformed shapes at end of loading for inviscid solutions. As can be seen, displacement contours show the diffused deformation patterns. However, to obtain the sharp localized deformation, we need to add a localization capability to the model and advance the solution into the softening-induced localization regime.

The load-displacement response of footing is plotted in Fig. 30. Slightly smaller values of the reaction force occur in the 1600-element mesh due to the increase in the number of degrees of freedom. The difference between the two meshes is small, however. The global Newton-Raphson convergence profile is illustrated in Tables 7 and 8. In this problem, an asymptotic rate of quadratic convergence is observed.

In order to attain further investigation, the stress path for the second integration point of two elements located under the right corner of the footing, is plotted on J_2^{ξ} vs. I_1 plane (Figs. 32 and 33). As seen in Fig. 33, the function G^{α}approaches to zero indicating that for element number 32, the translated yield surface meets the failure envelope. Thus, it is possible for that the point has experienced loss of ellipticity. Though it is beyond the scope of this paper, a bifurcation analysis [35] should be performed to ensure that the results not mesh dependent. This criterion has also been used to mark the onset of localized behavior, and can be coupled with an enhanced element [48] or another regularization technique to model the softening portion of the load-displacement curve. Such analysis is again beyond the scope of this paper, however.

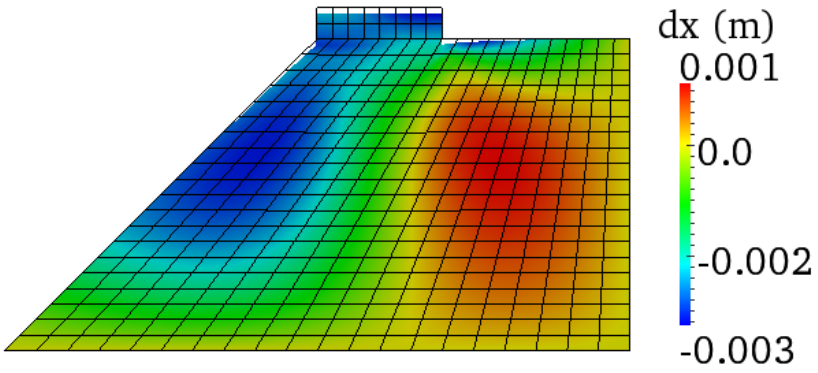

(a)

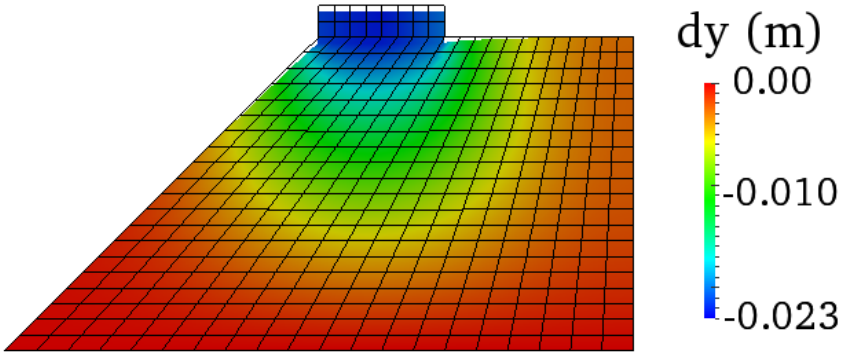

(b)

Fig. 28. Deformed shape for FE mesh with 400 linear quadrilateral elements: (a) horizontal displacement dx contours, (b) vertical displacement dy contours.

Table 7. Convergence of global algorithm for the slope stability problem with 400 elements

Norm of the global residual vector (d(m)) Number of n-r iterations = 4			
493.1531	9.3760e-03	6.8461e-06	2.4205e-09

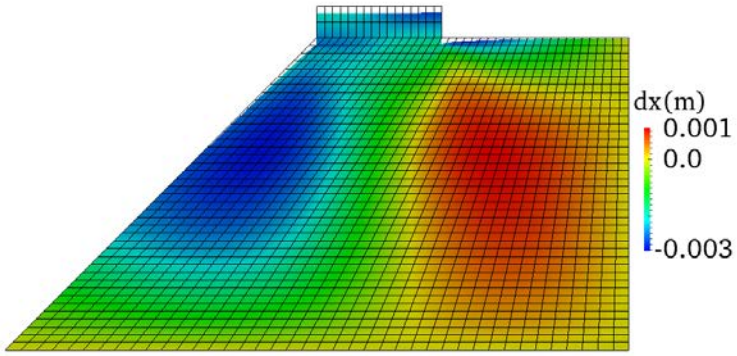

(a)

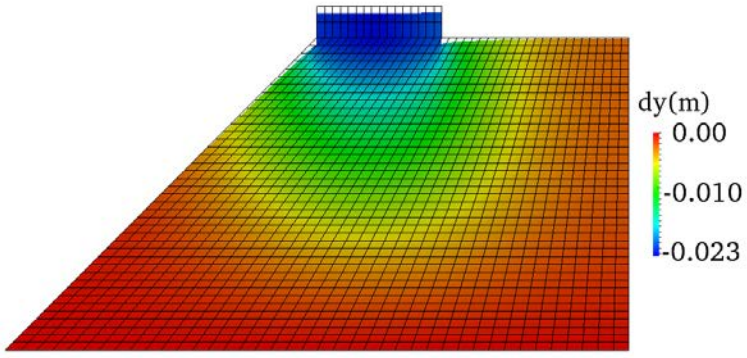

(b)

Fig. 29. Deformed shape for FE mesh with 1600 linear quadrilateral elements: (a) horizontal displacement dx contours, (b) vertical displacement dy contours.

Table 8. Convergence of global algorithm for the slope stability problem with 1600 elements

Norm of the global residual vector (d(m))			
Number of n-r iterations = 4			
307.2458	4.394973e-03	6.303301e-06	3.742939e-9

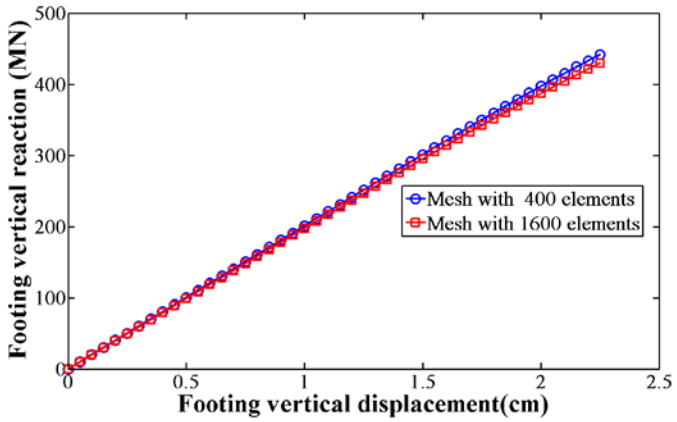

Fig. 30. Footing load-displacement plot for two FE meshes.

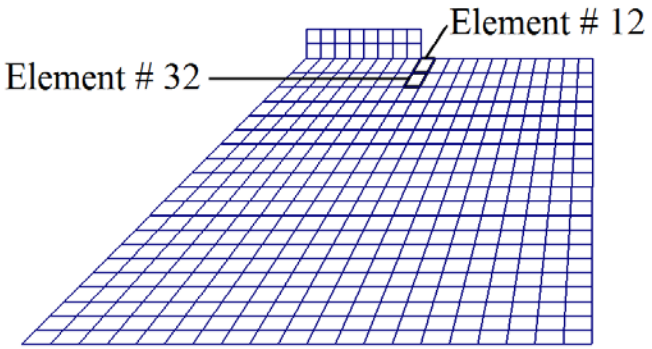

Fig. 31. FE mesh and selected elements (# 12 and 32) to draw stress path in meridional stress space.

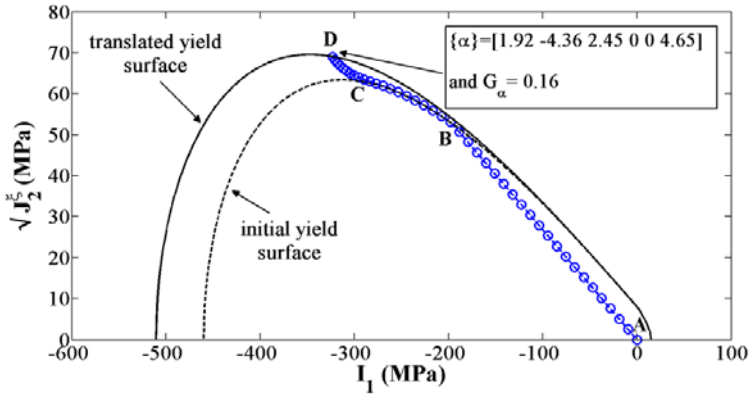

Fig. 32. Stress path in meridional stress space for the element # 12 at the integration point, IP=2. The letters indicate points on the stress path to distinguish different phases of evolution.

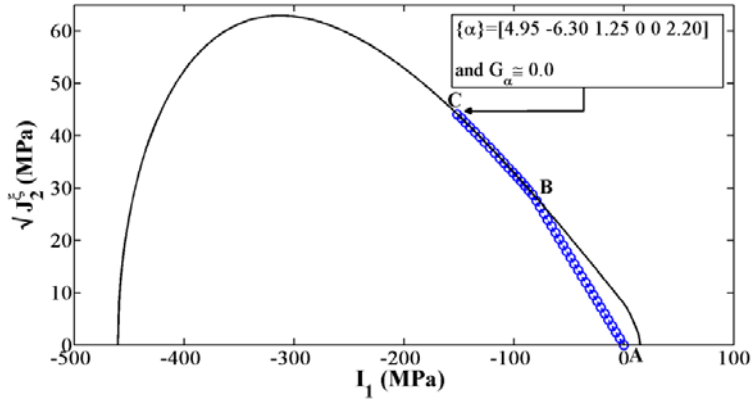

Fig. 33. Stress path in meridional stress space for a selected element # 32 at the integration point, IP=2. The letters indicate points on the stress path to distinguish different phases of evolution.

22 CONCLUDING REMARKS

In this work, a three-invariant elasto/viscoplastic model based on a non-associated flow rule and combined isotropic/kinematic hardening was developed. This modified model allows us to investigate complex mechanical behaviors of geomaterials under various loading conditions. Previous models have shown some lack of convergence in implicit numerical implementations, especially for large-scale problems. The relevant FE formulation using a fully implicit return-mapping algorithm is employed to solve fairly complicated nonlinear problems. In addition to spectral decomposition of the relative stress, the new shear/cap surface determination algorithm is presented to improve the numerical performance.

Several numerical examples including a large-scale BVP are presented to validate the robustness of the integration procedure and show the numerical algorithm exhibits quadratic rate of convergence. The simulation results demonstrate the ability of the model to capture several behaviors common to geomaterials including strain hardening, shear enhanced compaction, the Bauschinger effect, dilatancy, strain-rate sensitivity, nonassociativity, and differences in triaxial extension versus compression strength.

23 ACKNOWLEDGMENTS

This work was supported by the National University Rail Center (NURail), a US DOT-OST Tier 1 University Transportation Center. We gratefully acknowledge this support. In addition, the second author also gratefully acknowledges the support of NSF grant CMMI 1030398.

24 APPENDIX A:

We prove here that $\partial \mathrm{g}/\partial \mathrm{I}_1\,(\mathrm{I}_1^{\mathrm{tr}}, \kappa_{\mathrm{n}})$ has the same sign as $\partial \mathrm{g}/\partial \mathrm{I}_1\,(I_1, \kappa_{\mathrm{n+1}})$
First, we note:

$$tr\left(\frac{\partial g}{\partial \boldsymbol{\sigma}}\right) = \frac{\partial g}{\partial \sigma_{11}} + \frac{\partial g}{\partial \sigma_{22}} + \frac{\partial g}{\partial \sigma_{33}} = \frac{\partial g}{\partial \sigma_{ii}} \tag{A.1}$$

and

$$\frac{\partial g}{\partial I_1} = \frac{\partial g}{\partial \sigma_{ij}}\frac{\partial \sigma_{ij}}{\partial I_1} = \frac{\partial g}{\partial \sigma_{ij}}\delta_{ij} = \frac{\partial g}{\partial \sigma_{ii}} = tr\left(\frac{\partial g}{\partial \boldsymbol{\sigma}}\right) \tag{A.2}$$

From Eqs. (A.1) and (A.2), we can derive Eq. (A.3)

$$tr(\boldsymbol{\sigma}) = tr\left(\boldsymbol{\sigma}^{tr} - \Delta\gamma \boldsymbol{C}^{e} : \frac{\partial g}{\partial \boldsymbol{\sigma}}\right) \Rightarrow I_1 = I_1^{tr} - 3K\Delta\gamma tr\left(\frac{\partial g}{\partial \boldsymbol{\sigma}}\right) = I_1^{tr} - 3K\Delta\gamma\frac{\partial g}{\partial I_1} \tag{A.3}$$

The scalar internal state variable κ is not allowed to increase. In the case κ does change $\Delta\kappa = 3\Delta\gamma\left(\frac{\partial g}{\partial I_1}\right)/\left(\frac{\partial \varepsilon_v^p}{\partial X}\frac{\partial X}{\partial \kappa}\right)$. Hence, we can write

$$\kappa_{n+1} = \begin{cases} \kappa_n + \dfrac{3\Delta\gamma\left(\dfrac{\partial g}{\partial I_1}\right)}{\left(\dfrac{\partial \varepsilon_v^p}{\partial X}\dfrac{\partial X}{\partial \kappa}\right)}, & \partial g/\partial I_1 < 0 \\ \kappa_n \qquad\qquad , & \partial g/\partial I_1 \geq 0 \end{cases} \tag{A.4}$$

Since $\partial \varepsilon_v^p/\partial X$ and $\partial X/\partial \kappa$ are positive.
In the case $\frac{\partial g}{\partial I_1}(I_1, \kappa_{n+1}) > 0$, we can conclude that $I_1 < I_1^{tr}$(from Eq. A.3) and $\kappa_{n+1} = \kappa_n$(from Eq. A.4). Therefore, using the fact that $\partial^2 \mathrm{g}/\partial \mathrm{I}_1{}^2 \geq 0$ (refer to Appendix B), one can show

$$0 < \frac{\partial g}{\partial I_1}(I_1, \kappa_{n+1}) < \frac{\partial g}{\partial I_1}(I_1^{tr}, \kappa_{n+1}) = \frac{\partial g}{\partial I_1}(I_1^{tr}, \kappa_n) \tag{A.5}$$

Therefore, when $\frac{\partial g}{\partial I_1}(I_1, \kappa_{n+1}) > 0$, $\frac{\partial g}{\partial I_1}(I_1^{tr}, \kappa_n) > 0$. The contrapositive of this statement is
If $\frac{\partial g}{\partial I_1}(I_1^{tr}, \kappa_n) \leq 0$ then $\frac{\partial g}{\partial I_1}(I_1, \kappa_{n+1}) \leq 0$.
In the case that $\frac{\partial g}{\partial I_1}(I_1, \kappa_{n+1}) < 0$, we can conclude that $I_1^{tr} < I_1$ (from Eq. A.3) and $\kappa_{n+1} < \kappa_n$ (from Eq. A.4). Therefore, since $\partial^2 \mathrm{g}/\partial \mathrm{I}_1{}^2\, \partial\kappa \leq 0$ (refer to Appendix B), one can show that

$$\frac{\partial g}{\partial I_1}(I_1^{tr}, \kappa_n) \leq \frac{\partial g}{\partial I_1}(I_1^{tr}, \kappa_{n+1}) < \frac{\partial g}{\partial I_1}(I_1, \kappa_{n+1}) < 0 \tag{A.6}$$

Therefore, when $\frac{\partial g}{\partial I_1}(I_1, \kappa_{n+1}) < 0$, $\frac{\partial g}{\partial I_1}(I_1^{tr}, \kappa_n) < 0$. The contrapositive of this statement is
If $\frac{\partial g}{\partial I_1}(I_1^{tr}, \kappa_n) \geq 0$ then $\frac{\partial g}{\partial I_1}(I_1, \kappa_{n+1}) \geq 0$.

Hence, $\partial \mathrm{g}/\partial \mathrm{I}_1\ (\mathrm{I}_1^{\mathrm{tr}}, \kappa_{\mathrm{n}})$ has the same sign as $\partial \mathrm{g}/\partial \mathrm{I}_1\ (I_1, \kappa_{\mathrm{n+1}})$. The significance of this fact is that we can check whether $\frac{\partial g}{\partial I_1}(I_1^{tr}, \kappa_n)$ is negative. If it is, we include κ as a variable in our iterations. Otherwise, κ is fixed for set of iterations.

25 APPENDIX B:

We prove here that the second derivative with respect to I_1, $\partial^2 \mathrm{g}/\partial {\mathrm{I}_1}^2 \geq 0$ while the mixed derivative $\partial^2 \mathrm{g}/\partial \mathrm{I}_1\, \partial\kappa \leq 0$.
As shown below, signs of the aforementioned derivatives, Eqs. B.1a and B.2, are determined by checking and comparing the sign of each factor involved in calculations:

$$\frac{\partial^2 g}{\partial {I_1}^2} = {Term_1}^{\geq 0} + {Term_2}^{\geq 0} \tag{B.1a}$$

where

$$Term_1 = -\frac{1}{2{F_c}^{g \geq 0}}\left(\sqrt{{F_c}^{g}}\left[\frac{\partial^2 {F_c}^{g \leq 0}}{\partial {I_1}^2}\ ({F_f}^{g} - N)^{\geq 0} + \frac{\partial {F_c}^{g \geq 0}}{\partial I_1}\ \frac{\partial {F_f}^{g \leq 0}}{\partial I_1}\right] - \left[\frac{(\frac{\partial {F_c}^{g}}{\partial I_1})^2}{2\sqrt{{F_c}^{g}}}\ ({F_f}^{g} - N)^{\geq 0}\right]\right) \tag{B.1b}$$

$$Term_2 = -\left(\frac{\frac{\partial {F_c}^{g \geq 0}}{\partial I_1}\ \frac{\partial {F_f}^{g \leq 0}}{\partial I_1}}{2\sqrt{{F_c}^{g}}} + \frac{\partial^2 {F_c}^{g \leq 0}}{\partial {I_1}^2}\ \sqrt{{F_c}^{g}}\right) \tag{B.1c}$$

For the second quantity,

$$\frac{\partial^2 g}{\partial I_1 \partial \kappa}^{\leq 0} = -\frac{1}{2}\left(\left[\frac{\frac{\partial^2 {F_c}^{g \geq 0}}{\partial I_1 \partial \kappa}\ ({F_f}^{g} - N)^{\geq 0}\sqrt{{F_c}^{g}} - \frac{1}{2\sqrt{{F_c}^{g}}}\frac{\partial {F_c}^{g \geq 0}}{\partial I_1}\ \frac{\partial {F_c}^{g \leq 0}}{\partial \kappa}\ ({F_f}^{g} - N)^{\geq 0}}{{F_c}^{g \geq 0}}\right] + \left[\frac{\frac{\partial {F_f}^{g \leq 0}}{\partial I_1}\ \frac{\partial {F_c}^{g \leq 0}}{\partial \kappa}}{\sqrt{{F_c}^{g}}}\right]\right)^{\geq 0} \tag{B.2}$$

where

$$\frac{\partial^2 {F_c}^{g}}{\partial I_1 \partial \kappa} = 2H(\kappa - I_1)^{\geq 0}\left(\frac{(X^g - \kappa)^2 + 2(X^g - \kappa)^{\leq 0}(I_1 - \kappa)^{\leq 0}\left(\frac{\partial X^g}{\partial \kappa} - 1\right)^{\geq 0}}{(X^g - \kappa)^4}\right) \geq 0 \tag{B.3}$$

since

$$\frac{\partial X^g}{\partial \kappa} = 1 - Q\frac{\partial {F_f}^g(\kappa)}{\partial \kappa} \geq 1 \tag{B.4}$$

We also use the inequalities

$$\frac{\partial {F_f}^g}{\partial I_1} = -(LC\, exp(\, LI_1\,) + \varphi) \leq 0 \tag{B.5}$$

$$\frac{\partial {F_c}^g}{\partial \kappa} = 2H(\kappa - \, I_1)^{\geq 0}\left(\frac{(X^g - \, \kappa)^{\leq 0} + (I_1 - \, \kappa)^{\leq 0}\left(\frac{\partial X^g}{\partial \kappa} - 1\right)^{\geq 0}}{(X^g - \, \kappa)^2}\right)\left(\frac{I_1 - \, \kappa}{X^g - \, \kappa}\right)^{\geq 0} \leq 0 \tag{B.6}$$

$$\frac{\partial^2 {F_c}^g}{\partial {I_1}^2} = -2\left(\frac{H(\kappa - \, I_1)^{\geq 0}}{(X^g - \, \kappa)^2} + \frac{H(I_1 - \, I_1^T)^{\geq 0}}{(3T - \, I_1^T)^2}\right) \leq 0 \tag{B.7}$$

and

$$\frac{\partial {F_c}^g}{\partial I_1} = -2H(\kappa - \, I_1)^{\geq 0}\frac{(I_1 - \, \kappa)^{\leq 0}}{(X - \, \kappa)^2} - 2H(I_1 - \, I_1^T)^{\geq 0}\,\frac{(I_1 - \, I_1^T)^{\leq 0}}{(3T - \, I_1^T)^2} \geq 0 \tag{B.8}$$

Since $I_1 - \, \kappa \leq 0$ whenever $H(\kappa - \, I_1) \neq 0$, and similarly for the second term.

26 REFERENCES

[1] Estrada N, Lizcano A, Taboada A. Simulation of cemented granular materials. I. Macroscopic stress-strain response and strain localization. *Physical Review E.* 2010; **82**(1):1-11. doi:10.1103/PhysRevE.82.011303.

[2] Lim KW, Andrade JE. Granular element method for three-dimensional discrete element calculations, *International Journal for Numerical and Analytical Methods in Geomechanics* 2014; **38**:167–188. doi:10.1002/nag.2203.

[3] Zhao D, Nezami EG, Hashash YMA, Ghaboussi J. Three-dimensional discrete element simulation for granular materials, *Engineering Computations* 2006*;* **23**:749–770. doi:10.1108/02644400610689884.

[4] Topin V, Delenne JY, Radjai F, Brendel L, Mabille F. Strength and failure of cemented granular matter. *The European Physical Journal. E, Soft Matter* 2007; **23**:413–429. doi:10.1140/epje/i2007-10201-9.

[5] Delenne JY, Topin V, Radjai F. Failure of cemented granular materials under simple compression: experiments and numerical simulations. *Acta Mechanica* 2009; **205**:9–21. doi:10.1007/s00707-009-0160-9.

[6] Andrade JE, Tu X. Multiscale framework for behavior prediction in granular media. *Mechanics of Materials* 2009; **41**:652–669. doi:10.1016/j.mechmat.2008.12.005.

[7] Andrade JE, Avila CF, Hall SA, Lenoir N, Viggiani G. Multiscale modeling and characterization of granular matter: From grain kinematics to continuum mechanics. *Journal of the Mechanics and Physics of Solids* 2011; **59**:237–250. doi:10.1016/j.jmps.2010.10.009.

[8] Chen Q, Andrade JE, Samaniego E. AES for multiscale localization modeling in granular media. *Computer Methods in Applied Mechanics and Engineering* 2011; **200**:2473–2482. doi:10.1016/j.cma.2011.04.022.

[9] Dascalu C, Cambou B. Special issue: Multiscale Approaches to Geomaterials. *Acta Geotechnica* 2008; **3**:1–1. doi:10.1007/s11440-008-0054-3.

[10] Vernerey F, Liu WK, Moran B. Multi-scale micromorphic theory for hierarchical materials. *Journal of the Mechanics and Physics of Solids* 2007; **55**:2603–2651. doi:10.1016/j.jmps.2007.04.008.

[11] Tu X, Andrade JE, Chen Q. Return mapping for nonsmooth and multiscale elastoplasticity. *Computer Methods in Applied Mechanics and Engineering* 2009; **198**:2286–2296. doi:10.1016/j.cma.2009.02.014.

[12] Paterson MS, Wong T. Experimental Rock Deformation — The Brittle Field, in: Experimental Rock Deformation — The Brittle Field, Springer-Verlag, 2005; pp. i – x. doi:10.1007/b137431.

[13] Wong TF, Baud P. The brittle-ductile transition in porous rock: A review. *Journal of Structural Geology* 2012; **44**:25–53. doi:10.1016/j.jsg.2012.07.010.

[14] Abu Al-Rub RK, Darabi MK. A thermodynamic framework for constitutive modeling of time- and rate-dependent materials. Part I: Theory. *International Journal of Plasticity* 2012; **34**:61–92. doi:10.1016/j.ijplas.2012.01.002.

[15] Anandarajah A. Multi-mechanism anisotropic model for granular materials. *International Journal of Plasticity* 2008; **24**:804–846. doi:10.1016/j.ijplas.2007.07.012.

[16] Cecconi M, DeSimone A, Tamagnini C, Viggiani GMB. A constitutive model for granular materials with grain crushing and its application to a pyroclastic soil. *International Journal for Numerical and Analytical Methods in Geomechanics* 2002; **26**:1531–1560. doi:10.1002/nag.257.

[17] Darabi MK, Al-Rub RKA, Masad EA, Little DN. Thermodynamic-based model for coupling temperature-dependent viscoelastic, viscoplastic, and viscodamage constitutive behavior of asphalt mixtures. *International Journal for Numerical and Analytical Methods in Geomechanics 2012;* **36**:817–854. doi:10.1002/nag.1030.

[18] Sheldon HA, Barnicoat AC, Ord A. Numerical modelling of faulting and fluid flow in porous rocks: An approach based on critical state soil mechanics. *Journal of Structural Geology* 2006; **28**:1468–1482. doi:10.1016/j.jsg.2006.03.039.

[19] Navarro V, Alonso J, Calvo B, Sánchez J. A constitutive model for porous rock including effects of bond strength degradation and partial saturation. *International Journal of Rock Mechanics and Mining Sciences* 2010; **47**:1330–1338. doi:10.1016/j.ijrmms.2010.08.003.

[20] Tengattini A, Das A, Nguyen GD, Viggiani G, Hall SA, Einav I. A thermomechanical constitutive model for cemented granular materials with quantifiable internal variables. Part I—Theory. *Journal of the Mechanics and Physics of Solids* 2014; **70**:281–296. doi:10.1016/j.jmps.2014.05.021.

[21] DiMaggio FL, Sandler I.S. Material Model for Granular Soils. *Journal of the Engineering Mechanics Division* 1971; **97**:935–950.

[22] Desai CS, Siriwardane HJ. Constitutive laws for engineering materials with emphasis on geologic materials, Prentice-Hall, 1984.

[23] Grueschow E, Rudnicki JW. Elliptic yield cap constitutive modeling for high porosity sandstone. *International Journal of Solids and Structures* 2005; **42**:4574–4587. doi:10.1016/j.ijsolstr.2005.02.001.

[24] Lan YM, Sotelino ED, Chen WF. The strain-space consistent tangent operator and return mapping algorithm for constitutive modeling of confined concrete. *International Journal of Applied Science and Engineering* 2003; **1**:17–29.

[25] Lubarda VA, Mastilovic S, Knap J. Brittle-ductile transition in porous rocks by cap model. *Journal of Engineering Mechanics* 1996; **122**:633–642.

[26] Fossum AF, Brannon RM. The Sandia GeoModel: theory and user's guide, 2004.

[27] Kohler R, Hofstetter G. A cap model for partially saturated soils. I*nternational Journal for Numerical and Analytical Methods in Geomechanics* 2008; **32**:981–1004. doi:10.1002/nag.658.

[28] Karaoulanis FE. Implicit Numerical Integration of Nonsmooth Multisurface Yield Criteria in the Principal Stress Space, *Archives of Computational Methods in Engineering* 2013; **20**:263–308. doi:10.1007/s11831-013-9087-3.

[29] Borja RI. Plasticity: Modeling and Computation, Springer, 2013.

[30] Dolarevic S, Ibrahimbegovic A. A modified three-surface elasto-plastic cap model and its numerical implementation. *Computers & Structures* 2007; **85**:419–430. doi:10.1016/j.compstruc.2006.10.001.

[31] Fossum AF, Fredrich JT. Cap plasticity models and compactive and dilatant pre-fadure deformation, in: 4th North American Rock Mechanics Symposium, Balkema, 2000: pp. 1169–1176. http://www.osti.gov/bridge/product.biblio.jsp?osti_id=751348.

[32] Swan CC, Seo YK. A smooth, three-surface elasto-plastic cap model: Rate formulation, integration algorithm and tangent operators, 2000.

[33] DorMohammadi H, Khoei AR. A three-invariant cap model with isotropic–kinematic hardening rule and associated plasticity for granular materials. *International Journal of Solids and Structures* 2008; **45**:631–656. doi:10.1016/j.ijsolstr.2007.08.019.

[34] Foster CD, Regueiro RA, Fossum AF, Borja RI. Implicit numerical integration of a three-invariant, isotropic/kinematic hardening cap plasticity model for geomaterials. *Computer Methods in Applied Mechanics and Engineering* 2005; **194**:5109–5138. doi:10.1016/j.cma.2005.01.001.

[35] Regueiro RA, Foster CD. Bifurcation analysis for a rate-sensitive, non-associative, three-invariant, isotropic/kinematic hardening cap plasticity model for geomaterials: Part I. Small strain. *International Journal for Numerical and Analytical Methods in Geomechanics* 2011; **35**:201–225. doi:10.1002/nag.907.

[36] Sun W, Chen Q, Ostien JT. Modeling the hydro-mechanical responses of strip and circular punch loadings on water-saturated collapsible geomaterials. *Acta Geotechnica* 2013; **9**:903-934. doi:10.1007/s11440-013-0276-x.

[37] Simo J, Hughes T. Computational Inelasticity, XIV, Springer, 1998.

[38] Kindrachuk VM, Galanov BA. An efficient approach for numerical treatment of some inequalities in solid mechanics on examples of Kuhn–Tucker and Signorini–Fichera conditions. *Journal of the Mechanics and Physics of Solids* 2014; **63**:432–450. doi:10.1016/j.jmps.2013.08.008.

[39] Tamrakar SB, Mitachi T, Toyosawa Y, Itoh K. Development of a New Soil Tensile Strength Test Apparatus, in: Site Characterization and Modeling. American Society of Civil Engineers, Reston, VA, 2005: pp. 1–10. doi:10.1061/40785(164)26.

[40] Lu N, Wu B, Tan CP, Tensile strength characteristics of unsaturated sands. *Journal of Geotechnical and Geoenvironmental Engineering* 2007; **133**:144–154. doi:http://dx.doi.org/10.1061/(ASCE)1090-0241(2007)133:2(144).

[41] Collins I. Associated and non-associated aspects of the constitutive laws for coupled elastic/plastic materials. *International Journal of Geomechanics* 2002; **2**:259–267. doi:10.1080/15323640208500176.

[42] Hjiaj M, Fortin J, de Saxcé G. A complete stress update algorithm for the non-associated Drucker–Prager model including treatment of the apex. *International Journal of Engineering Science* 2003; **41**:1109–1143. doi:10.1016/S0020-7225(02)00376-2.

[43] Zhu QZ, Shao JF, Mainguy M, A micromechanics-based elastoplastic damage model for granular materials at low confining pressure, *International Journal of Plasticity* 2010; **26**:586–602. doi:10.1016/j.ijplas.2009.09.006.

[44] McDowell DL. Viscoplasticity of heterogeneous metallic materials, Materials Science and Engineering: R: Reports 2008; **62**:67–123. doi:10.1016/j.mser.2008.04.003.

[45] Baud P, Schubnel A, Wong T. Dilatancy, compaction, and failure mode in Solnhofen limestone. *Journal of Geophysical Research* 2000; **105**:289–303. doi:10.1029/2000JB900133.

[46] Einav I, Breakage mechanics—Part I: Theory. *Journal of the Mechanics and Physics of Solids* 2007; **55**:1274–1297. doi:10.1016/j.jmps.2006.11.003.

[47] Das A, Tengattini A, Nguyen GD, Viggiani G, Hall S, Einav I. A thermomechanical constitutive model for cemented granular materials with quantifiable internal variables. part II – validation and localization analysis. *Journal of the Mechanics and Physics of Solids* 2014; **70**:382-405 doi:10.1016/j.jmps.2014.05.022.

[48] Foster CD, Borja RI, Regueiro RA. Embedded strong discontinuity finite elements for fractured geomaterials with variable friction. *International Journal for Numerical Methods in Engineering* 2007; **72**:549–581. doi:10.1002/nme.2020.

[49] GAJO A, Multiple shear band development and related instabilities in granular materials, *Journal of the Mechanics and Physics of Solids* 2004; **52**:2683–2724. doi:10.1016/j.jmps.2004.05.010.

[50] Borja RI, Song X, Rechenmacher AL, Abedi S, Wu W. Shear band in sand with spatially varying density. *Journal of the Mechanics and Physics of Solids* 2013; **61**:219–234. doi:10.1016/j.jmps.2012.07.008.

[51] Duvaut G, Lions LJ, Les inéquations en mécanique et en physique, Paris, Dunod., 1972.

[52] Simo JC, Taylor RL. Consistent tangent operators for rate-independent elastoplasticity. *Computer Methods in Applied Mechanics and Engineering* 1985; **48**:101–118. doi:10.1016/0045-7825(85)90070-2.

[53] Borja RI, Sama KM, Sanz PF. On the numerical integration of three-invariant elastoplastic constitutive models. *Computer Methods in Applied Mechanics and Engineering* 2003; **192**:1227–1258. doi:10.1016/S0045-7825(02)00620-5.

[54] Tamagnini C, Castellanza R, Nova R. A Generalized Backward Euler algorithm for the numerical integration of an isotropic hardening elastoplastic model for mechanical and chemical degradation of bonded geomaterials. *International Journal for Numerical and Analytical Methods in Geomechanics* 2002; **26**:963–1004. doi:10.1002/nag.231.

[55] McDowell GR, Bolton MD, Robertson D. The fractal crushing of granular materials, *Journal of the Mechanics and Physics of Solids* 1996; **44**:2079–2101. doi:10.1016/S0022-5096(96)00058-0.

[56] Curran JH, Carroll MM. Shear stress enhancement of void compaction. *Journal of Geophysical Research* 1979; **84** (B3):1105-1112. doi:10.1029/JB084iB03p01105.

[57] Dautriat J, Gland N, Dimanov A, Raphanel J. Hydromechanical behavior of heterogeneous carbonate rock under proportional triaxial loadings. *Journal of Geophysical Research* 2011; **116** (B01205):1-26. doi:10.1029/2009JB000830.

[58] Klein E, Baud P, Reuschlé T, Wong T. Mechanical behaviour and failure mode of bentheim sandstone under triaxial compression. *Physics and Chemistry of the Earth, Part A: Solid Earth and Geodesy* 2001; **26**:21–25. doi:10.1016/S1464-1895(01)00017-5.

[59] Vajdova V. Compaction, dilatancy, and failure in porous carbonate rocks. *Journal of Geophysical Research* 2004; **109** (B5):1-16. doi:10.1029/2003JB002508.

[60] Xie SY, Shao JF. Elastoplastic deformation of a porous rock and water interaction. *International Journal of Plasticity* 2006; **22**:2195–2225. doi:10.1016/j.ijplas.2006.03.002.

36 [61] Xie SY, Shao JF. Experimental investigation and poroplastic modelling of saturated porous geomaterials. *International Journal of Plasticity* 2012; **39**:27–45. doi:10.1016/j.ijplas.2012.05.007. .